Materials Characterization 209 (2024) 113768

Contents lists available at ScienceDirect

Materials Characterization

journal homepage: www.elsevier.com/locate/matchar

Effect of compositional variations on the heat treatment response in 17-4 PH stainless steel fabricated by laser powder bed fusion

M.S. Moyle [a], N. Haghdadi [a,*], F. Theska [a], M.P. Haines [a], X.Z. Liao [b,c], S.P. Ringer [b,c], S. Primig [a,*]

[a] School of Materials Science & Engineering, UNSW Sydney, NSW 2052, Australia
[b] Australian Centre for Microscopy & Microanalysis, The University of Sydney, NSW 2006, Australia
[c] School of Aerospace, Mechanical and Mechatronic Engineering, The University of Sydney, NSW 2006, Australia

ARTICLE INFO

Keywords:
Additive manufacturing
Stainless steel
Precipitation
Atom probe tomography

ABSTRACT

17–4 precipitate hardening (PH) stainless steel is used in various applications including in the aerospace, marine, and chemical industries, largely due to its unique combination of corrosion resistance and high strength, which is achieved by the formation of nanoscale Cu-rich precipitates during aging. 17–4 PH has been widely researched for its applicability for laser powder bed fusion (LPBF). However, there are discrepancies in the literature on its heat treatment response, which seem to be linked to compositional variations. Systematic studies of the interplay between these variations and nanoscale precipitation are currently missing. Using atom probe tomography, we present a systematic study of the heat treatment responses of two variants of LPBF 17–4 PH builds fabricated from different powder feedstocks, with significant differences in N contents (High vs Low N 17–4). Both variants formed predominantly δ-ferritic as-built microstructures. The as-built High N 17–4 variant showed a higher volume fraction of austenite which further increased upon solution annealing and quenching. The consequence was no appreciable hardening effect due to the absence of Cu precipitation in either austenite or martensite after aging, degrading the alloy's desirable property profile. Conversely, Low N 17–4 showed no austenite in the as-built condition and a fully martensitic matrix after solution annealing. This variant had the desired aging response; a ~ 140 HV 5 increase in hardness due to nanoscale Cu precipitation. Our findings describe the deleterious effects of compositional variations incurred during the LPBF process flow and how they can be overcome in 17–4 PH and similar steels.

1. Introduction

17–4 precipitate hardening (PH) stainless steel processed by conventional cast and wrought routes is a martensitic stainless steel with excellent corrosion resistance with high strength and toughness up to 315 °C with applications in the aerospace, marine, and chemical processing industries [1–3]. More recently, it has been the centre of much additive manufacturing (AM) research owing to these desirable properties as well as its high weldability, making it suitable for fabrication via laser powder bed fusion (LPBF) [4–6]. Its precipitate hardening properties are resultant from the formation of nanoscale Cu-rich precipitates (CRPs) within the martensitic matrix [2,7,8]. The established heat treatment procedure for 17–4 PH after conventional processing requires a solution heat treatment at 1040 °C followed by a water quench to form a martensitic microstructure with a random distribution of alloying elements in solid solution [9,10]. This heat treatment is referred to as the condition A (CA) treatment. Following this, an aging treatment is applied to form the CRPs. It has been well established that the highest strength will be achieved by aging at 480 °C for 1 h (also referred to as the H900 heat treatment) [2,9]. Whilst investigating cast and wrought 17–4 PH, studies utilising atom probe tomography (APT) and transmission electron microscopy have shown that continued aging will cause a reduction in strength as the CRPs coarsen and undergo crystallographic changes from B2 → body centred cubic (BCC) → 9R → face centred cubic (FCC) [11,12]. It has also been shown that overaging of cast and wrought 17–4 PH results in the co-precipitation of a second type of precipitates primarily enriched in Ni, Mn, and Si referred to as NMS precipitates [10,13]. If and to what extent co-precipitation behaviour takes place in the peak aged condition after LPBF remains unknown.

After the fabrication of 17–4 PH via LPBF, different groups of researchers have reported vastly different phase constitutions of the

* Corresponding authors.
E-mail addresses: nima.haghdadi@unsw.edu.au (N. Haghdadi), s.primig@unsw.edu.au (S. Primig).

https://doi.org/10.1016/j.matchar.2024.113768
Received 16 October 2023; Received in revised form 5 February 2024; Accepted 12 February 2024
Available online 13 February 2024
1044-5803/© 2024 The Authors. Published by Elsevier Inc. This is an open access article under the CC BY license (http://creativecommons.org/licenses/by/4.0/).

matrix microstructure, ranging from 0 to 100% martensite, [4,5,14,15] leading to significant differences in the mechanical properties [16]. In some cases, rapid solidification has resulted in a mainly δ-ferrite (ferrite in the following) microstructure rather than martensite [14,15]. It should be noted that the typical C content (< 0.07 wt% [17]) in 17–4 PH is so low that both martensite and ferrite exhibit BCC crystal structures, with the consequence that these phases cannot easily be differentiated via diffraction based methods [14]. Facchini et al. [5] reported a 78% volume fraction of austenite within the room temperature as-built microstructure of LPBF fabricated 17–4 PH. Furthermore, some studies have reported that a 100% martensitic microstructure is not achieved after the CA heat treatment [18,19]. This is contrary to other groups of researchers investigating LPBF 17–4 PH [14,20] as well as its typical cast and wrought behaviour [2,7]. It is reasonable to attribute this to compositional variations due to differences between 17 and 4 PH powder feedstocks used. Additionally, compositional variations induced during the LPBF process flow, such as the incorporation of the atomising or cover gas and selective vaporisation of more volatile alloying elements from the melt pool, may also have an effect [1,21]. These changes will affect the relative stability of austenite, ferrite, or martensite in this steel, as reflected in the Schaeffler diagram, originally developed for welding [22,23]. The detailed evolution of the matrix microstructure will have an effect on the heat treatment response as Cu has different solubilities and diffusivities in different phases. However, systematic studies of the effects of such compositional variations on the heat treatment response of 17–4 PH are currently unavailable.

The presence of a high fraction of austenite within the microstructure has a pronounced and well-known effect on the mechanical properties of 17–4 PH. This is because austenite is the softest matrix phase [23] and may transform to martensite under mechanical loading, resulting in the transformation induced plasticity (TRIP) effect [18,20]. Furthermore, high fractions of austenite have been shown to inhibit the effects of aging heat treatments on the mechanical properties [20,24]. Since austenite has a higher solubility for Cu than either ferrite or martensite, it has been postulated that a high volume fraction of austenite would result in Cu remaining in solid solution in the FCC austenite phase rather than forming precipitates upon aging [8,20,24,25]. The absence of precipitation in the austenite with precipitation in martensite/ferrite has been observed experimentally in other precipitate hardening steels [26,27]. To the best of the authors' knowledge, this has not yet been validated by systematic nanoscale APT studies of both the FCC and BCC phases. The aim of this research is to provide the first systematic study of the interplay between compositional variations during LPBF of 17–4 PH and their impact on the nanoscale precipitation and heat treatment response. We examine two 17–4 PH LPBF variants with significant differences in N contents. This leads to different phase transformation pathways in the as-built conditions and following post-build heat treatments. We use correlative microscopy and APT to better understand the microstructural mechanisms determining the formation or absence of CRPs.

2. Materials and methods

Two different variants of 17–4 PH builds were manufactured by LPBF using two different powder feedstocks and LPBF machines. The two variants of LPBF 17–4 PH will be referred to as High N 17–4 and Low N 17–4 in the following due to their significant differences in N contents.

High N 17–4 builds were printed as 10 mm × 10 mm × 15 mm cuboids in an atmosphere of N_2 gas using a 3D Systems ProX 300 LPBF machine, as also outlined in [15]. The powder was provided by 3D systems. Its composition was evaluated by inductively coupled plasma atomic emission spectroscopy (ICP-AES) and is given in Table 1. The LECO method was used to accurately determine the N composition. No preheating was applied to the build plate. The scanning strategy used was a bidirectional scan rotated 90° on and off between alternating build layers. In this strategy, the bidirectional laser scan pattern was broken up into sequentially scanned hexagonal islands which measured 50 mm between opposite vertices. The laser power was 161.5 W, the scanning speed 1200 mm s^{-1}, the hatch spacing 50 μm, and the layer height 40 μm.

Low N 17–4 samples were printed as 10 mm × 10 mm × 20 mm cuboids in an Ar atmosphere using an MLAB 200R LPBF machine. This powder was supplied by GE. Its composition was also analysed via ICP-AES and is provided in Table 1. For these builds, the scanning strategy was also a bidirectional scan rotated 90° on and off between alternating build layers but without the use of any island scan. Here, the laser power was 130 W, the scanning speed 1170 mm s^{-1}, the hatch spacing 82 μm, and the layer height 30 μm. It should be noted that the slight differences in scanning patterns and other LPBF parameters between the two variants studied here are due to the different capabilities of the respective LPBF systems. However, we attempted to create as similar as possible conditions.

Table 1 also shows the Cr_{eq}/Ni_{eq} ratios resulting from the compositions measured via ICP-AES. The Cr_{eq}/Ni_{eq} ratio is a compositional

Table 1
Compositions of the powders and builds for the two variants of 17–4 PH used in this study as determined by ICP-AES analysis. Calculated Cr_{eq}/Ni_{eq} ratios are provided. The difference in N composition between the two variants has the most significant effect on the Cr_{eq}/Ni_{eq} ratio (underlined).

	Fe	C	Mn	Si	S	P	Ni	Cr	Mo	Cu	V	Nb	Ti	Al	N	Cr_{eq}/Ni_{eq}
wt%																
High N 17–4																
Powder	73.49	0.03	0.87	0.71	<0.01	0.03	4.34	16.1	0.13	3.81	0.04	0.32	0.02	0.01	0.10	1.99
Build	72.19	0.02	0.90	0.92	<0.01	0.03	4.57	16.8	0.12	3.92	0.06	0.37	<0.01	0.01	0.09	2.19
Low N 17–4																
Powder	73.88	0.02	0.64	0.57	<0.01	0.03	4.01	16.5	0.08	3.88	<0.01	0.34	0.02	0.01	0.02	2.79
Build	74.41	0.01	0.67	0.77	0.01	0.01	4.31	17.0	0.02	3.55	<0.01	0.22	<0.01	<0.01	0.02	2.91
at.%																
High N 17–4																
Powder	72.40	0.14	0.87	1.39	<0.02	0.05	4.07	17.04	0.07	3.30	0.04	0.19	0.02	0.02	0.39	
Build	71.01	0.09	0.90	1.80	<0.02	0.05	4.28	18.01	0.07	3.39	0.06	0.22	<0.01	0.02	0.35	
Low N 17–4																
Powder	73.05	0.09	0.64	1.12	<0.02	0.05	3.77	17.52	0.05	3.37	<0.01	0.20	0.02	0.02	0.08	
Build	72.39	0.05	0.67	1.51	0.02	0.02	4.04	18.01	0.01	3.08	<0.01	0.13	<0.01	<0.02	0.08	

expression evaluating the stability of austenite vs ferrite/martensite in steels, with lower Cr_{eq}/Ni_{eq} ratios indicating a greater stability of austenite. These values were calculated from the following Eqs. [28]:

$$Cr_{eq}\ (wt\%) = Cr + 2(Si) + 1.5(Mo) + 5(V) + 5.5(Al) + 1.75(Nb) + 1.5(Ti) + 0.75(W) \quad (1)$$

$$Ni_{eq}\ (wt\%) = Ni + (Co) + 0.5(Mn) + 0.3(Cu) + 25(N) + 30(C) \quad (2)$$

Although Table 1 shows that there are a number of elements which have different compositional values in the two variants, the difference in N content has the greatest effect on the difference in Cr_{eq}/Ni_{eq} ratios between the two builds, hence why these builds are referred to as High N 17–4 and Low N 17–4 in this work.

After fabrication, various samples were tested in different heat treatment conditions: (1) The as-built condition (AB), where the intrinsic heat treatment (IHT) of the LPBF process has been the effective thermal history; (2) Post-fabrication solution annealing treatment at 1040 °C for 1 h followed by a water quench (CA); and (3) After heat treating to CA followed by an aging treatment at 480 °C for 1 h followed by air cooling (CA-H900). Heat treatments were performed in air using a Nabertherm LHTCT 03/16/C550 high temperature furnace. Fig. 1 shows the thermal cycles experienced by each of these samples schematically.

Electron backscattered diffraction (EBSD) was performed after grinding samples to a final grit of 4000 using SiC paper, polishing using 3 μm then 1 μm diamond suspensions, followed by electropolishing at 25 V for 30 s using the Struers A2 electrolyte. Electropolishing ensured that no mechanical preparation induced phase transformation of the matrix occurred within the scanned area. EBSD data was collected in a JEOL 7001f SEM using an EDAX Hikari Super camera. The scans were acquired using an accelerating voltage of 20 kV, a probe current of 13 nA, and a 6 × 6 binning. The data was collected using the EDAX-OIM EBSD suite. The TSL OIM 8.0 software was used for data processing.

Standard (non-site-specific) atom probe tomography (APT) tips were fabricated by cutting 0.5 mm × 0.5 mm blanks from various samples and then sharpening via a two-step electropolishing process using perchloric acid via the double layer method then the "micro-loop" method, as outlined by Gault et al. [29]. APT was performed on these tips using a CAMECA Local Electrode Atom Probe (LEAP) 3000 Si in voltage mode, with a detection efficiency of 57%. A temperature of 50 K, a pulse rate of 200 kHz, a pulse fraction of 20%, and a target evaporation rate of 0.5% were used.

Site-specific APT specimens (e.g., containing phase boundaries) were fabricated via the use of focussed ion beam (FIB) and in-situ lift-out using an FEI Helios G4 Xe^+ plasma-FIB (PFIB). PFIB was used in conjunction with transmission Kikuchi diffraction (TKD) to ensure that the selected regions of interest were captured in subsequent APT analysis [30]. To ensure the absence of FIB related artefacts in subsequent correlative analysis, some additional tips were prepared by the standard electropolishing procedure described above before also undergoing to TKD analysis. After TKD, the prepared tips were then subjected to APT using a CAMECA LEAP 4000X Si in laser mode to reduce the probability of in-situ tip fracture [30]. The temperature was set to 45 K, and a pulse rate of 200 kHz, a laser energy of 50 pJ, and a target evaporation rate of 1.0% were used. The detection efficiency was 57%.

A STRUERS Duramin-40 AC3 Vickers hardness tester was used to collect hardness data from bulk regions of samples, with sufficient distance from build surfaces. A load of 5 kg and a dwell time of 15 s were applied. Hardness results were averaged from 10 indents. It was ensured that the size of the indents under this load covered a sufficient area to give results representative of the whole microstructure in each sample.

Equilibrium compositions of matrix phases, matrix phase volume fractions, and diffusivities were calculated using ThermoCalc® with the TCFE11 and MOBFE6 databases. ICP-AES determined compositions of the 17–4 PH builds in Table 1 were used as input data.

3. Results and discussion

In the first part of this section, the individual microstructural evolution of the High N 17–4 variant is discussed followed by that of the Low N 17–4 variant. In the second part of this section, differences between the two variants are assessed and discussed based on the literature and a schematic model.

3.1. High N 17-4: Lower Cr_{eq}/Ni_{eq} ratio

Fig. 2 shows the microstructural evolution in the High N 17–4 samples in each heat-treated condition considered here. The inverse pole figure (IPF) maps (Fig. 2a, e, i) show the grain size and structure, evolution and the phase maps (Fig. 2b, f, j) show the BCC vs FCC phase fractions and distributions. Cu atom maps (Fig. 2c, g, k) and Cu 1st Nearest Neighbour (NN) distributions (Fig. 2d, h, l) reveal the behaviour of Cu within regions subjected to non-site-specific APT analysis. Based on the morphology of the grains indexed as BCC in Fig. 2a and b, showing epitaxial growth patterns around the bidirectional hatch of the melt pool structure, it is determined that the as-printed microstructure consists primarily of δ-ferrite, as detailed in previous work [15]. There is also a minor volume fraction of austenite found within the matrix

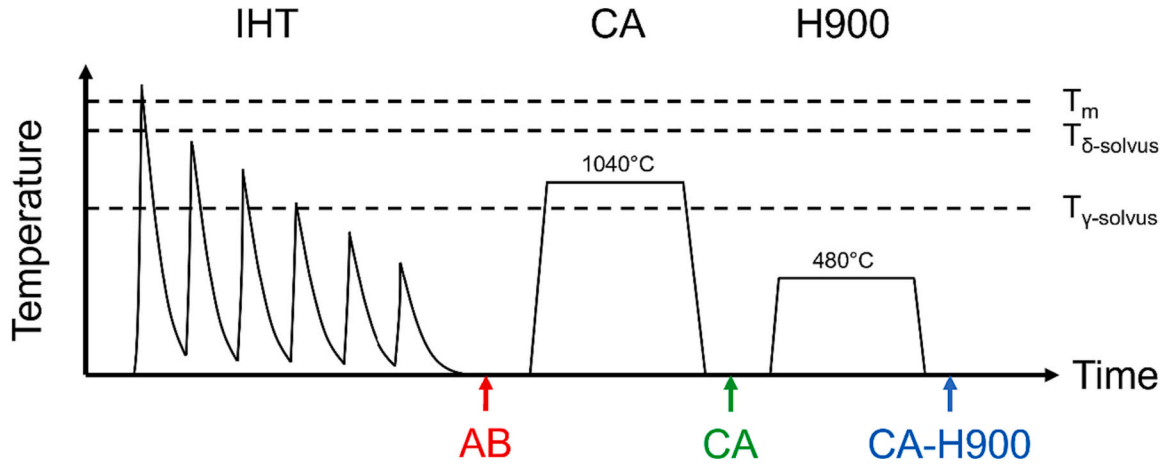


Fig. 1. Schematic diagram showing the thermal histories of samples considered in this research. Above the axis, the thermal cycles are labelled: Intrinsic heat treatment (IHT) during LPBF fabrication, the condition A heat treatment (CA), and the H900 heat treatment. Below the axis, the heat treatment conditions of samples considered in this study are indicated. T_m, $T_{\delta\text{-solvus}}$, and $T_{\gamma\text{-solvus}}$ indicate the melting, δ-ferrite solvus, and the γ-austenite solvus temperatures, respectively.

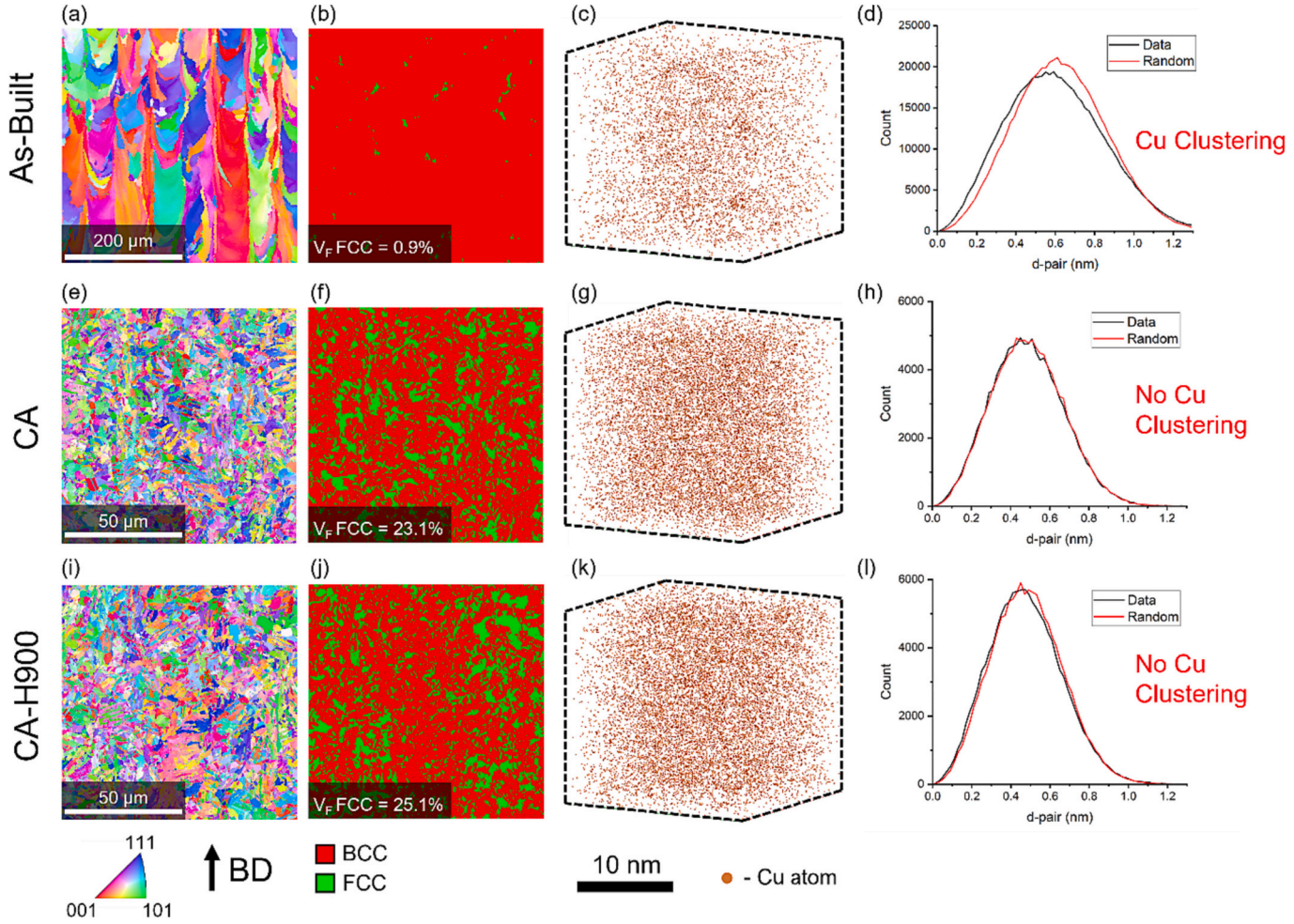


Fig. 2. Microstructural evolution of High N 17–4 samples through the (a-d) as-built state, (e-h) CA, and (i-l) CA-H900 conditions. EBSD data showing (a,e,i) IPF maps showing orientation along BD, (b,f,j) phase maps with the volume fractions (V_F) of FCC by area quoted. Non-site-specific APT data showing (c,g,k) Cu atom map with $20 \times 20 \times 20$ $(nm)^3$ selections of datasets. (d,h,l) Cu 1st nearest neighbour distributions from the entire APT datasets (black) compared to a randomised distribution (red). BD indicates the build direction. (For interpretation of the references to colour in this figure legend, the reader is referred to the web version of this article.)

microstructure (0.9% according to EBSD). Comparing Fig. 2a and e, the change in grain size and morphology resultant from the CA heat treatment is clear. The lath structure BCC indexed in the IPF maps for the CA and CA-H900 samples demonstrates that this phase is martensite formed by the CA heat treatment. Comparing the Cu 1st NN distributions to randomised distributions (Fig. 2d, h, l) provides qualitative, visual evidence of Cu clustering within the APT datasets. Different subfigures have different magnitudes for count due to the different sizes of the datasets collected. Fig. 2h and l demonstrate that the Cu 1st NN distributions align well with randomised distributions, showing that the distribution of Cu becomes randomised during the CA heat treatment and remains random after aging (CA-H900). However, it can be seen in Fig. 2d that the Cu 1st NN distribution skews to shorter distances (d-pair lengths) in the as-built dataset, demonstrating that Cu atoms are, on average, closer to one another than they would be if their positions were random. This evidence of co-segregation means that the Cu atoms in the dataset have diffused towards one another. This demonstrates the occurrence of Cu clustering under the effect of the IHT of the LPBF process [31,32]. This level of Cu clustering can be seen visually comparing the subsections of the three datasets in Fig. 2c, g, and k. Nearest neighbour analyses reveal that all other elements within these APT datasets exhibit random distributions. For brevity, their distributions are not shown here, and are instead presented in the supplementary material (Fig. S 1).

Based on the literature, it is expected that some level of Cu clustering or precipitation is present in as-built AM samples as a result of the IHT, and that these features are removed by the homogenising CA heat treatment [2]. However, the H900 aging treatment is designed to ensure the maximum level of strengthening in 17–4 PH via the formation of CRPs [2,9]. Therefore, the lack of any Cu clustering or precipitation in the CA-H900 samples (Fig. 2l) is undesirable and contrary to both expectations and the results of aging conventionally processed 17–4 PH in literature [10,13,33]. Furthermore, the increase in the volume fraction of austenite after the CA heat treatment is also contrary to expectations, as this heat treatment is designed to result in a microstructure of nearly 100% martensite, supersaturated in Cu [7,34]. The presence of a high volume fraction of austenite after the CA heat treatment, also observed in LPBF 17–4 PH literature [35,36], is plausibly due to the composition of the powder used, presented in Table 1. If the powder is enriched in austenite forming elements, resulting in a lower Cr_{eq}/Ni_{eq} ratio, then austenite will have a greater stability [18,22,35], resulting in its strong retention in the microstructure. Table 1 also shows that there is a difference in composition between the High N 17–4 powder and the High N 17–4 LBPF build. This is likely due to the selective evaporation of certain elements [21]. Among the elements that shifted in composition, the change in Cr had the most significant effect on the Cr_{eq}/Ni_{eq} ratio, leading to an increase from 1.99 to 2.19 during LPBF.

To understand the effect of austenite on the segregation behaviour of Cu and other alloying elements in LPBF fabricated 17–4 PH, site-specific APT was carried out on regions containing FCC/BCC phase boundaries. Fig. 3 shows a TKD/APT analysis for the as-built sample. Two different

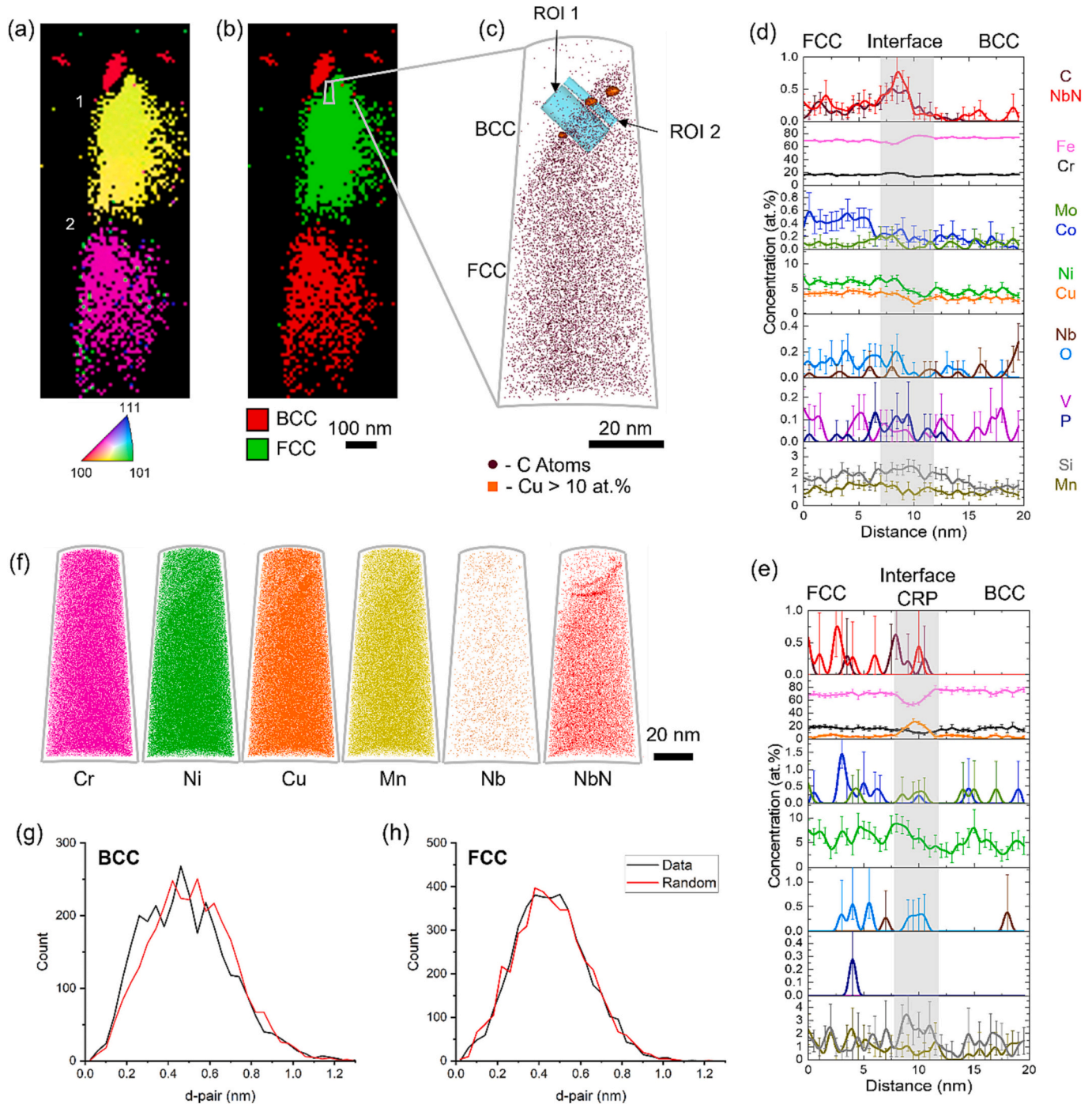


Fig. 3. TKD and subsequent APT analysis of a High N 17–4 as-built APT tip targeting an FCC/BCC phase boundary. (a) IPF orientation map along the length of the tip, and (b) phase map. (c) APT atom map showing the distribution of C atoms and isosurfaces of >10 at.% Cu and two cylindrical regions of interest (ROIs) across the interface. (d,e) 1-dimensional (1D) concentration profile across the interface from the ROIs in (c) Avoiding CRPs (ROI 1), and passing through a CRP (ROI 2), respectively. (f) Additional atom maps. (g,h) 1st nearest neighbour distributions for Cu, as compared to randomised distributions from the (g) BCC and (h) FCC regions of the dataset.

FCC/BCC phase boundaries were captured in the tip via TKD, which are labelled as "1" and "2" in Fig. 3a. Boundary 1 is close to the Nishiyama-Wasserman (N-W) orientation relationship ($\{111\}_\gamma$ // $\{110\}_\alpha$, $\langle 112\rangle_\gamma$ // $\langle 110\rangle_\alpha$) [37,38] and boundary 2 aligns well with the Pitsch orientation relationship ($\{100\}_\gamma$ // $\{110\}_\alpha$, $<110>_\gamma$ // $\langle 111\rangle_\alpha$) [39]. Given that both boundaries show a good alignment with established orientation relationships, it cannot be determined which ferrite grain (red or pink in Fig. 3a) the austenite grain nucleated from during the LPBF process.

In Fig. 3c, the phase boundary is apparent by the clear segregation of C to the austenite phase. It is known that segregation artefacts may arise in APT data where no segregation exists in the sample due to the surface migration effect [40]. However, such segregation artefacts present along the poles and zone and are aligned with the length of the dataset. As the atomic segregation observed in Fig. 3c-f has no such pattern or alignment, it is not generated by this aberration effect and is, therefore, true elemental segregation that exists within the sample. A value of 10 at.% Cu was chosen to define the CRPs based on previous reports in literature [10]. Fig. 3c clearly shows that CRPs have formed along the FCC/BCC

phase boundaries during LPBF fabrication rather than in the interior of either phase.

Upon re-evaluating a dataset from a sample that had exactly the same processing conditions containing a phase boundary in a previous study [31], it is found that CRPs are also observed to form along the phase boundary, consistent with the observations made in Fig. 3. This shows the repeatability of the observations made here, giving strong evidence that it is the general behaviour of Cu to precipitate on the FCC/BCC phase boundaries during LPBF fabrication of High N 17–4 samples.

For the dataset considered in Fig. 3, regions of interest (ROIs) of equal volumes (not shown in Fig. 3) within both phases of this dataset, away from the phase boundary, were examined to quantify differences in atomic distributions. Based on these regions, the Cu 1st NN distributions for both the BCC and FCC grains are given in Fig. 3g and Fig. 3h, respectively. As compared to Fig. 2d, h, and l, a greater level of noise is present in Fig. 3g and Fig. 3h due to the much lower number of atoms captured in these regions of interest. Despite this, the BCC phase clearly shows a greater level of Cu clustering than the FCC phase. This gives evidence for a phenomenon that has previously been hypothesised and discussed in the literature; that a 17–4 PH system with a duplex matrix would show greater Cu clustering behaviour in BCC than in FCC [2,8,20,25]. These results are significant as, to the best of the authors' knowledge, this has not been experimentally demonstrated in a duplex system. It is believed that this is due to the greater solubility of Cu in an FCC Fe matrix than in BCC [25]. Furthermore, the diffusivity of Cu in austenite is $\sim 10^3$ times lower (varying with temperature) than in ferrite [25]. This means that, when in solid solution in austenite, Cu has less of a tendency to form a precipitate phase and the kinetics of the formation of such precipitates are much slower than they would be in a BCC matrix. The selective absence of precipitation behaviour in austenitic regions of the matrix has been observed by Jägle et al. [27] who used APT to investigate the as-built microstructure of AM 300 maraging steel, showing Ti and Mo based nano-precipitates in martensite with an adjacent austenite grain devoid of any precipitates.

Fig. 3f shows characteristic atom maps, highlighting the partitioning of Ni, Cu, Mn, C, and N to the austenite phase. Unfortunately, N partitioning within datasets of 17–4 PH is difficult to quantify. The peaks within the mass spectrum of 17–4 PH associated with N as monoatomic ionic species are eclipsed by peaks resultant from Si ions with the same mass charge ratio [40]. Given that the amount of Si in the 17–4 PH material considered in this study is much larger than the amount of N (see Table 1), the proportions of the observed peaks that can be attributed to N are negligible. However, distinct peaks within the mass spectrum can be attributed to NbN ions as well as independent Nb ions. By observing the differences in the ion distribution maps for Nb and NbN in Fig. 3f, the partitioning behaviour of N (i.e., the ratios of N concentration between austenite and ferrite) can still be surmised. A similar approach to determining the behaviour of N was used by Yeli et al. [13]. However, without the ability to range isolated N peaks in the mass spectrum, the absolute concentrations of N quoted in these datasets are proportional underestimates. Linear regions enriched in NbN can be seen leading away from the phase boundary into the ferrite phase, perhaps indicating dislocations that N has diffused to [13].

Fig. 3c shows cylindrical ROIs through the phase boundary within the as-built dataset, one avoiding any interface CRPs (ROI 1) and one going through an interface CRP (ROI 2). Fig. 3d and e show the compositional profiles along ROI 1 and ROI 2, respectively. It can be seen in Fig. 3d that the FCC phase is more enriched in C, N, Ni, Cu, O, and Co and that the BCC phase is more enriched in Fe. Furthermore, several elements show enrichments or depletions at the boundary itself. C, N, Cr, and Mo all show an enrichment towards the FCC side of the phase boundary. Fe shows a depletion in concentration towards the FCC side of the phase boundary and an enrichment towards the BCC side. The equilibrium compositions of both the BCC and FCC matrix phases were evaluated in ThermoCalc® at a temperature of 677 °C (950 K), the temperature at which there is predicted to be an equal equilibrium volume fraction of each phase considering the composition of the High N 17–4 LPBF build. This was to ensure that relative solubility was the main factor governing compositional differences between the phases, avoiding saturation effects as much as possible. The results, shown in Table 2, are consistent with the partitioning of elements to the different phases in the as-built condition in Fig. 3d. Beyond this, the interstitial elements C and N have a greater presence at the interface itself. This is expected as these elements have a distinctly greater grain boundary enrichment ratio in BCC Fe, largely correlating with a reduced solubility with the matrix and a tendency to reduce the grain boundary energy [41,42].

Comparing Fig. 3d and e, the most notable difference between regions of the phase boundary with and without the presence of a CRP is that the concentration of Cu increases at the CRP at the expense of a drop in the concentrations of Fe and Cr. Analyses of elements at lower compositions become more difficult in the 1D concentration profile going through the CRP due to the ROI cylinder's smaller radius, so as to ensure that only the precipitate is analysed at the boundary. This means that, per unit distance, the compositional profile captures a lower volume of material. The effect is an increase in the compositional error, which has a proportionally greater impact on the low concentration elements.

Fig. 4 shows correlative TKD/APT results for the High N 17–4 sample aged to the CA-H900 condition after LPBF fabrication. An FCC/BCC phase boundary was identified using EBSD before PFIB was employed to isolate this boundary. During TKD of the resultant tip, it was observed that the FCC region had transformed to BCC, likely due to a mechanical transformation induced by the ion milling process, an effect previously observed and characterised by Seo et al. [43]. This is why both grains on either side of the boundary in Fig. 4b are indexed as BCC. Crystallographic analysis confirming that the BCC martensite laths in Fig. 4b did indeed transform from the selected FCC austenite grain via the Kurdjumov-Sachs orientation relationship [44] can be found in the supplementary material (Fig. S 2). Given that the mechanically induced austenite to martensite transformation is displacive, subsequent APT results relating to the composition variations through the FCC/BCC phase boundary will not have been affected by this phase change [23].

As for the phase boundary in the as-built sample (shown in Fig. 3), Fig. 4c shows that CRPs also form at the FCC/BCC phase boundaries in the CA-H900 sample. However, no CRPs are observed to have formed in the bulk of either grain, contrary to the typical behaviour of 17–4 PH after aging treatments [10,13]. Furthermore, the Cu nearest neighbour distributions presented in Fig. 4g and h do not show any pronounced clustering in either grain. This absence of Cu segregation within the bulk of grains is consistent with the notion that the presence of significant volume fractions of austenite within 17–4 PH inhibits the formation of CRPs [20,24]. However, Hsu et al. [24] have suggested that aging a duplex 17–4 PH microstructure would result in Cu precipitates forming within the BCC phase but not in the FCC phase. Conversely, Fig. 4g and h show that there is no evidence of precipitation in either phase of the

Table 2
Equilibrium compositions (in at.%) of BCC and FCC matrix phase as determined by ThermoCalc® using the ICP-AES determined composition of the High N 17–4 LPBF build at a temperature of 677 °C (950 K).

Element	BCC	FCC
Fe	86.6	73.5
C	1.31×10^{-5}	5.93×10^{-5}
Mn	0.613	1.3
Si	2.23	1.83
Ni	2.81	6.36
Cr	24.7	15.8
Mo	0.0979	0.0591
Cu	0.308	1.09
V	0.118	0.0337
Nb	0.122	0.0573
Ti	1.37×10^{-4}	3.40×10^{-5}
Al	0.0318	0.013
N	7.57×10^{-7}	1.67×10^{-5}

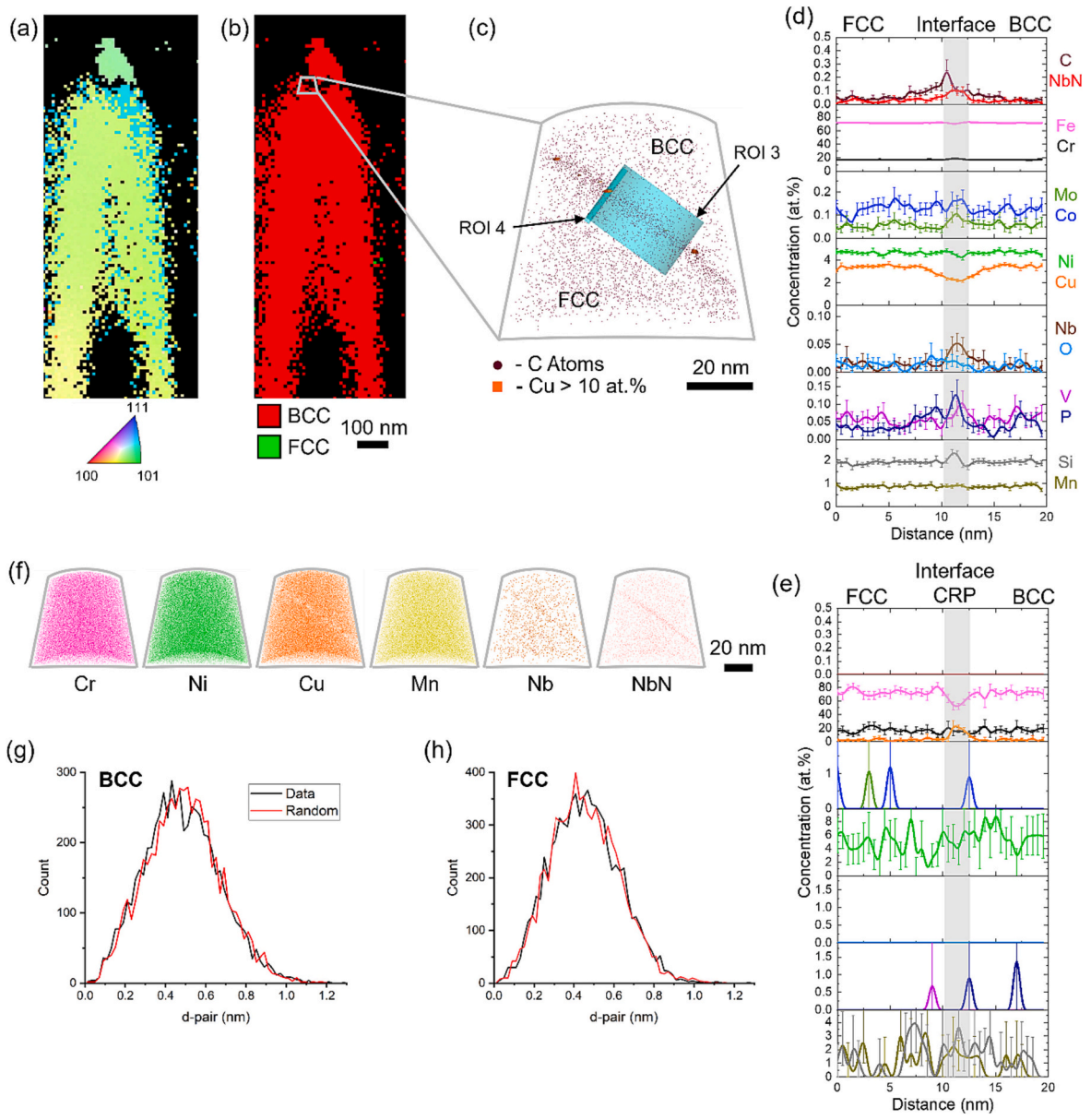


Fig. 4. TKD and subsequent APT analysis of a High N 17–4 CA-H900 APT tip targeting an FCC/BCC phase boundary. (a) IPF orientation map along the length of the tip, and (b) phase map. (c) APT atom map showing the distribution of C atoms and isosurfaces of >10 at.% Cu and two cylindrical regions of interest (ROIs) across the interface. (d,e) 1-dimensional (1D) concentration profile across the interface from the ROIs in (c) Avoiding CRPs (ROI 3), and passing through a CRP (ROI 4), respectively. (f) Additional atom maps. (g,h) 1st nearest neighbour distributions for Cu, as compared to randomised distributions from the (g) BCC and (h) FCC regions of the dataset.

duplex CA-H900 High N 17–4 sample. The absence of precipitation in the BCC phase of the High N 17–4 sample in the CA-H900 condition was confirmed by additional correlative analysis presented in the supplementary material (Fig. S 3). SEM, TKD, and APT were performed on tips that were prepared by electropolishing, eliminating any possibility of phase misidentification due any FCC to BCC transformation induced by ion-milling. Using TKD to ensure that the APT data came from BCC regions of the sample, all additional tips confirmed the absence of any strong Cu clustering or precipitation behaviour in BCC regions of the sample.

The atom maps presented in Fig. 4f highlight segregation effects along the boundary. These effects are further quantified by the compositional profiles through the boundary. Two ROIs across the boundary are shown in Fig. 4c with one avoiding any CRPs and one going through a selected CRP. Compositional profiles from these ROIs are presented in Fig. 4d and Fig. 4e, respectively. Avoiding the CRPs, Fig. 4d shows that there is a local enrichment of C, N, Mo, P, and Si at the boundary as well as a depletion in Cu. There is also an enrichment in Cr and a depletion in Fe, though these are much lower relative to the overall concentrations of these elements. Going through the CRP, an enrichment of Cu and a depletion of Fe were observed. Similar to Fig. 3e, due to the small size of CRPs in this dataset, this narrower region of interest was not able to provide sufficient data relating to the lower concentration elements for meaningful analysis. It is clear that the concentration of Cu is depleted at the boundary as well as in the matrix regions approaching the boundary. This shows that Cu has diffused from the matrix to the CRPs present along the interface. This is likely due to faster diffusion occurring at the interfaces due to imperfect crystallographic packing in these regions [41,45,46]. Additionally, the interfacial energy of the boundary will provide more favourable nucleation sites for the formation of secondary phases, such as CRPs [47].

3.2. Low N 17-4: Higher Cr_{eq}/Ni_{eq} ratio

Similar to the High N 17-4, the Cr_{eq}/Ni_{eq} ratio of the Low N 17-4 increases during the LPBF process, from 2.79 to 2.91, as shown in Table 1. Fig. 5 shows EBSD maps from the Low N 17-4 samples in three different heat treatment states. Although different powder feedstocks were used, the IPF map for the as-built condition shown in Fig. 5a reveals a comparable BCC grain structure to those shown for the "hexagonal low-power" samples in our previous work on High N 17–4 builds [15]. This is due to the similar process parameters used as well as an

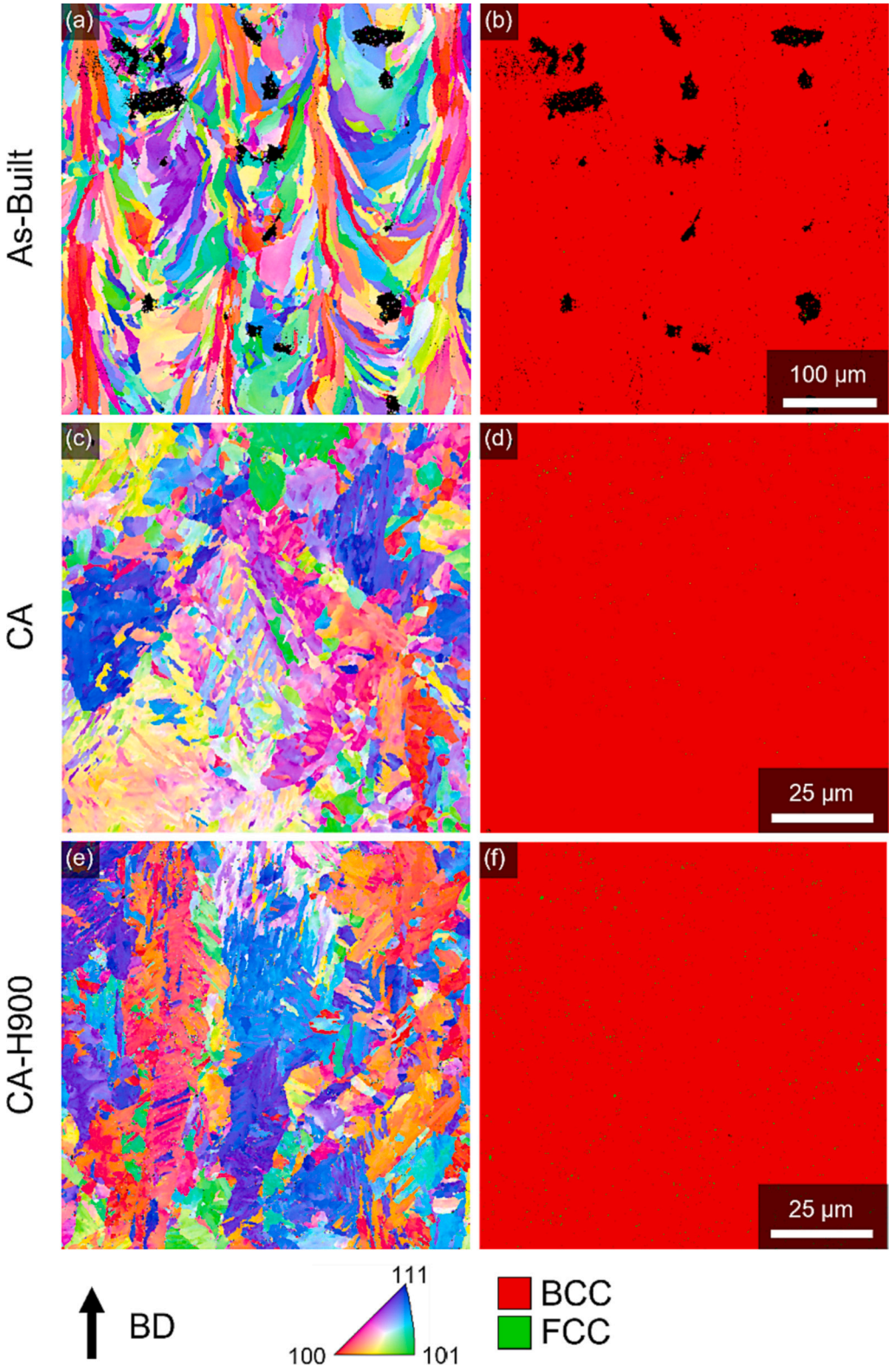


Fig. 5. EBSD maps from Low N 17–4 samples in the (a,b) as-built, (c,d) CA, (e,f) CA-H900 conditions. (a,c,e) IPF maps showing orientation along BD, (b,d,f) phase maps. Data from the as-built condition in (a,b) was threshold based on confidence index to exclude pores from analysis.

alternating 90° rotation within the scan layers. However, the phase map in Fig. 5b shows an almost completely BCC microstructure in the as-built state within the resolution limits of the EBSD scan. This contrasts to the results in [15] where periodic regions of austenite within the microstructure were found. Furthermore, the microstructure within these samples is BCC in crystallographic structure after the CA and CA-H900 heat treatments, showing that aging did not result in any significant austenite reversion. This contrasts to the post CA heat treatment phase fractions in the High N 17–4 samples, shown in Fig. 2f and j, likely due to the greater Cr_{eq}/Ni_{eq} ratio of the Low N 17–4 powder. Comparing Fig. 5a and Fig. 5c reveals that the CA heat treatment results in a refinement of the microstructure as well as the transition from an LPBF melt-pool based solidification δ-ferrite microstructure to a martensitic packet/lath microstructure.

Fig. 6 shows APT data from the as-built sample. The atom distribution maps in Fig. 6a show segregation of C, Nb, and N at the top and bottom of the dataset. These regions are highlighted by the C isoconcentration surfaces in Fig. 6b. These are likely due to the presence of carbides. Fig. 6c shows the presence of distinct Cu precipitates. It is noted that the distribution of these precipitates is not random within the dataset. This is likely due to the surface migration effect whereby the concentrations of certain atomic species, in this case Cu, are enhanced along certain crystallographic directions and diminished along others [40]. As the Cu isosurfaces form as distinct precipitates, not a single column, the surface migration effect has not created the appearance of precipitates where there is in reality no clustering/precipitation behaviour. The CRPs shown on the right of Fig. 6c may have a lower true Cu concentration, but equally the diminishment of Cu to the left may mask CRPs that would otherwise have a sufficient concentration to generate isoconcentration surfaces. Fig. 6d shows a proxigram through the Cu isoconcentration surfaces, which shows the enrichment of Cu at the interior of the indexed CRPs at the expense of Fe and all other alloying elements. Fig. 6e shows the Cu 1st NN distribution of Cu atoms within this dataset in black, with a randomised distribution shown in red. This shows the degree of Cu clustering/precipitation in the as-built state for the Low N 17–4 samples, which is greater than that of the High N 17–4 as-built samples (Fig. 2d), as indicated by the greater offset between the data and randomised distributions.

Fig. 7 shows APT data from the Low N 17–4 build heat treated to condition A. No segregation of any species is apparent in the atom maps in Fig. 7a. The Cu 1st NN distribution is shown against a randomised distribution in Fig. 7b. These graphs align well with each other showing that the distribution of Cu atoms within the dataset is random as a result of the CA heat treatment, having eliminated the clustering/precipitation present in the as-built state (Fig. 6c-e) as expected. The CRPs present in the as-built microstructure dissolve in austenite during the heat treatment and remain in a random distribution after the austenite transforms into martensite during quenching [10,13].

Fig. 8 shows APT data from the CA-H900 sample. The atom maps, presented in Fig. 8a, show clear elemental segregation. Cu precipitates are visible, as is desired, as well as globular concentrated regions of Ni, Mn, and Nb. Elongated regions of high concentration are present in the NbN ion map, presumably showing N segregation to dislocation lines due to their misfit with the lattice [45] as is also observed in the ferrite phase of Fig. 3f. Fig. 8b shows the Cu 1st NN distribution for this dataset. Due to the formation of these precipitates, it can be seen that the average

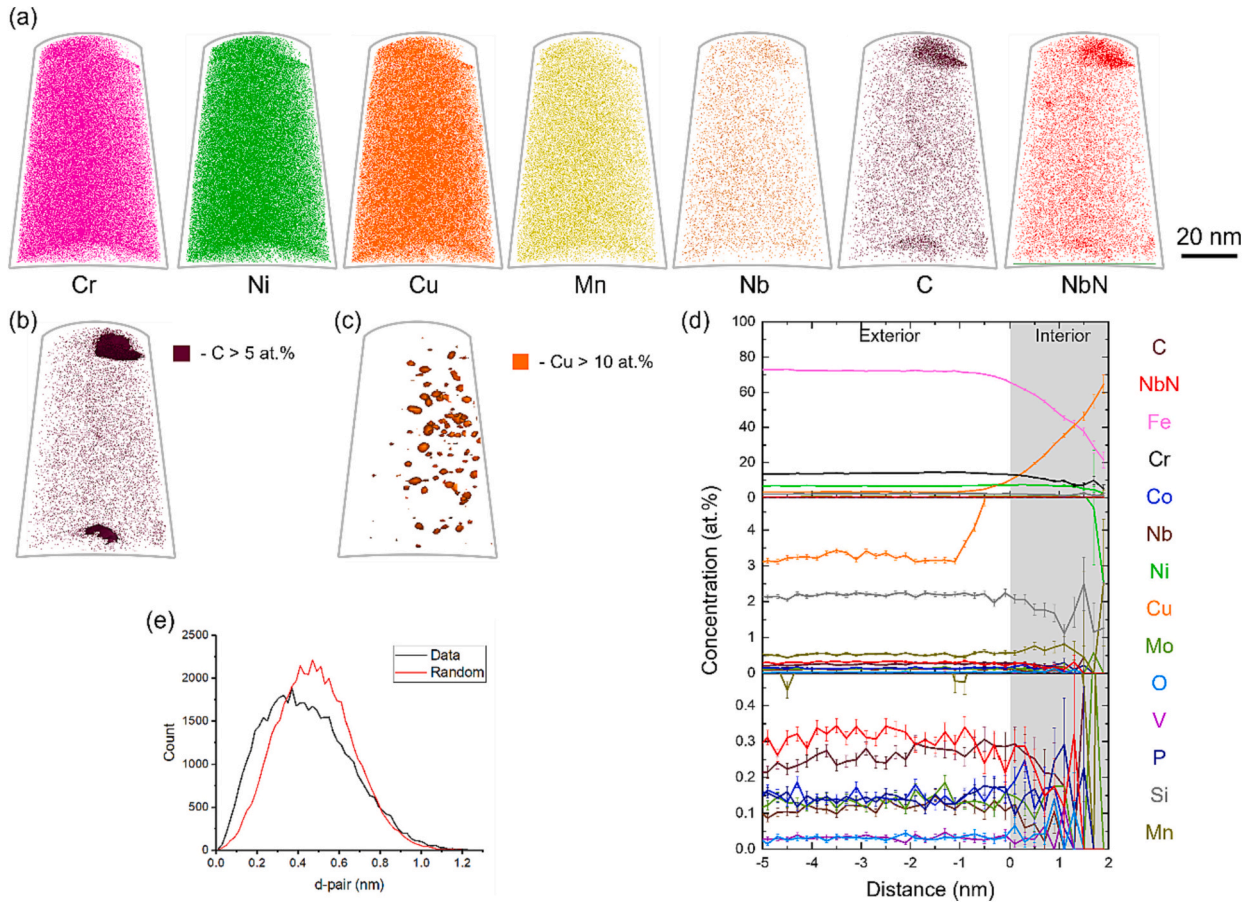


Fig. 6. APT data from the Low N 17–4 as-built sample. (a) Atom maps, (b) C atom map with C > 5 at.% isoconcentration surface, (c) Cu > 10 at.% isoconcentration surfaces, (d) concentration proxigram of the Cu isoconcentration surface, (e) Cu nearest neighbour distribution (black) compared to a randomised distribution (red) considering a spherical ROI excluding the C > 5 at.% isosurface regions. (For interpretation of the references to colour in this figure legend, the reader is referred to the web version of this article.)

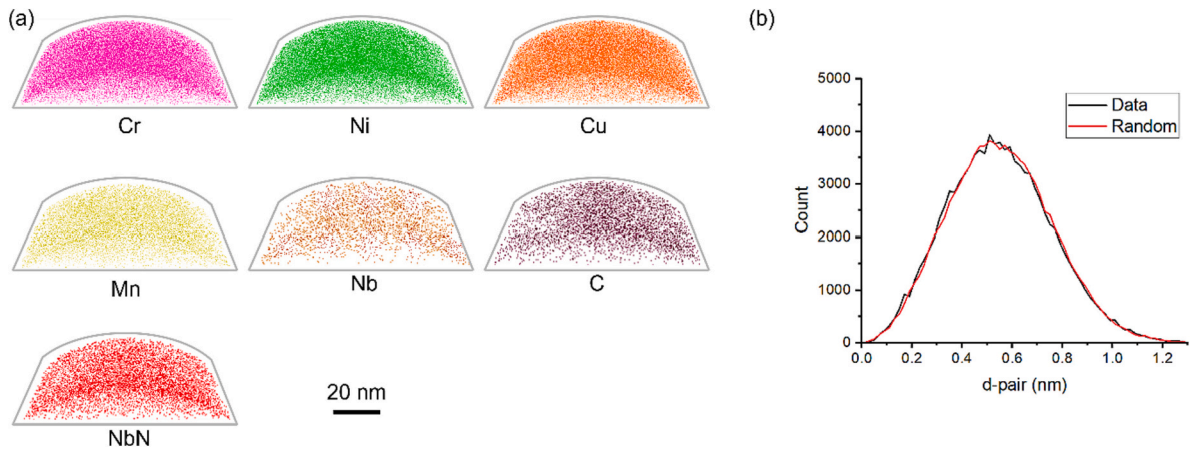


Fig. 7. APT data from the Low N 17–4 sample heat treated to condition A. (a) Atom maps, and (b) Cu nearest neighbour distribution (black) compared to a randomised distribution (red). (For interpretation of the references to colour in this figure legend, the reader is referred to the web version of this article.)

Cu 1st NN displacement is much shorter than for a randomised dataset. Examining Fig. 6, Fig. 7b, and Fig. 8b, the degree of Cu precipitation resulting from the H900 treatment becomes apparent and is much more extensive than the Cu precipitation in the as-built state, which is only resultant from the IHT.

Fig. 8c shows two types of isoconcentration surfaces within the dataset; Cu $>$ 10 at.% in orange and Ni + Mn + Si $>$ 15 at.% in dark green. This data is evidence for the presence of two compositionally distinct types of precipitates within the dataset; CRPs and NMS precipitates (Ni, Mn, Si enriched). NMS precipitates were neither observed to form adjacent to CRPs present in the Low N 17–4 as-built sample (Fig. 6c) nor at the interface CRPs in the High N 17–4 as-built and CA-H900 samples (Fig. 3c and Fig. 4c, respectively). As CRPs grow during continued aging, becoming more enriched in Cu, they undergo crystallographic changes (B2 → BCC → 9R → FCC) [11,12]. It is known that CRPs take on an ellipsoidal shape after the transformation to an FCC structure due to the anisotropic surface energy of different crystallographic interfaces formed with the matrix [48]. From the high degree of sphericity of the CRPs displayed in Fig. 8c, it is surmised that the 9R → FCC transformation has not yet taken place, meaning that the CRPs in this build are either coherent B2, BCC or 9R. An FCC structure is only expected to develop in the precipitates after prolonged over aging, well beyond the H900 condition [10,48]. Within this dataset, assuming a perfectly spherical morphology, the average diameter of the CRPs is 3.8 nm, and the average number density is 1.30×10^{23} m^{-3} based on the indexed Cu isosurfaces. Comparing this with the absence of any CRPs in either grain of the High N 17–4 CA-H900 samples following the same heat treatment (Fig. 4), underscores that Cu precipitation within grains during aging has been completely inhibited in the High N 17–4. The observation of some, but not all, CRPs forming NMS co-precipitates is consistent with previous studies on wrought 17–4 PH [10]. By the alignment of precipitates in the lower portion of the dataset, a lath boundary is clearly visible. An ROI (ROI 5) across this boundary is also shown in Fig. 8c. Fig. 8d shows the 1D concentration profile along this ROI. It can be seen that there is no strong difference in concentration between the two lath interiors except for a slight increase in Fe and decrease in Cr between the bottom and top laths. However, along the lath boundary, a number of compositional fluctuations can be identified. There is a marked increase in the concentrations of N, Cu, Ni, Mn, Si, and Co as well as a decrease in Fe. There is also a marked depletion of Cu on either side of this peak. This is likely because much of the Cu has been locally incorporated into CRPs which formed predominantly along the lath boundary due to a lower heterogeneous nucleation energy and faster local diffusion [41,45,46].

Fig. 9 shows additional analyses performed along the lath boundary present in the APT dataset for Low N 17–4 in the CA-H900 condition (Fig. 8) to ascertain the degree of segregation along the lath boundary occurring outside discrete precipitates. Fig. 9a and b show the position of an ROI (ROI 6) going across the lath boundary but avoiding any precipitates on the lath boundary itself indicated by the Cu and NiMnSi isoconcentration surfaces. Fig. 9c shows the concentration profile along ROI 6. The most significant enrichment at the lath boundary is N. Other elements show local enrichments (Cu, Ni) and depletions (Fe) which are lower in magnitude compared to other local enrichments captured in ROI 6 away from the lath boundary, at the sites of precipitates in the lath interiors. However, the distinct presence of Cu enrichments at the boundary, away from defined precipitates, contrasts with the behaviour at the phase boundary of High N 17–4 in the CA-H900 condition (Fig. 4), which shows a depletion of Cu at the boundary outside regions where CRPs have formed. The Cu concentration profile in Fig. 9c shows that the matrix concentration of Cu is ~0 at.% outside locally enriched areas up to and including precipitates. This further highlights the degree to which Cu atoms have diffused towards one another in the Low N 17–4 sample following the CA-H900 heat treatment.

Fig. 8e and Fig. 8f show proxigrams resulting from the Cu and NiMnSi isoconcentration surfaces, respectively. Fig. 8e shows that Cu is the only element that reaches its peak concentration at the centre of the CRPs. It can be seen that the Cu concentration in the CA-H900 material is very low immediately outside the CRPs but increases at greater distances from the precipitate. Comparing this with Fig. 6d, which shows a proxigram through the same Cu isoconcentration surfaces in the as-built Low N 17–4 structures, outside the CRPs, the Cu concentration is homogeneous. This highlights the extent of Cu precipitation after the CA-H900 heat treatment. The aging time has allowed for a greater diffusion of Cu, resulting in greater peak concentrations within and a lower matrix concentration of Cu outside the precipitates. The absence of any other elemental concentration peaks in Fig. 6d is because the IHT was not sufficient to result in the formation of NMS co-precipitates/clusters in the as-built condition. However, Fig. 8f shows that, at the centre of the NMS precipitates, the concentrations of Ni, Si, Mn, Nb, N, P, Mo, and C show peaks. Wang et al. [10] performed proxigram analyses on CRPs in APT datasets of wrought 17–4 PH aged at 450 °C for 8 h and 36 h. Compared to the current Fig. 8e, their results shows the enrichment of the same elements inside the precipitates with the exception of Nb, which was reported to have no significant change in concentration between the matrix and CRPs, and Mo, which showed a decrease in concentration within the CRPs in their study. The opposite trend is observed in the data presented here.

Fig. 10 shows concentration profiles taken through precipitates within the CA-H900 dataset. Fig. 10a shows the location of a cylindrical ROI (ROI 7) going through a CRP/NMS co-precipitate. Fig. 10b demonstrates the variation of concentration of selected elements along ROI

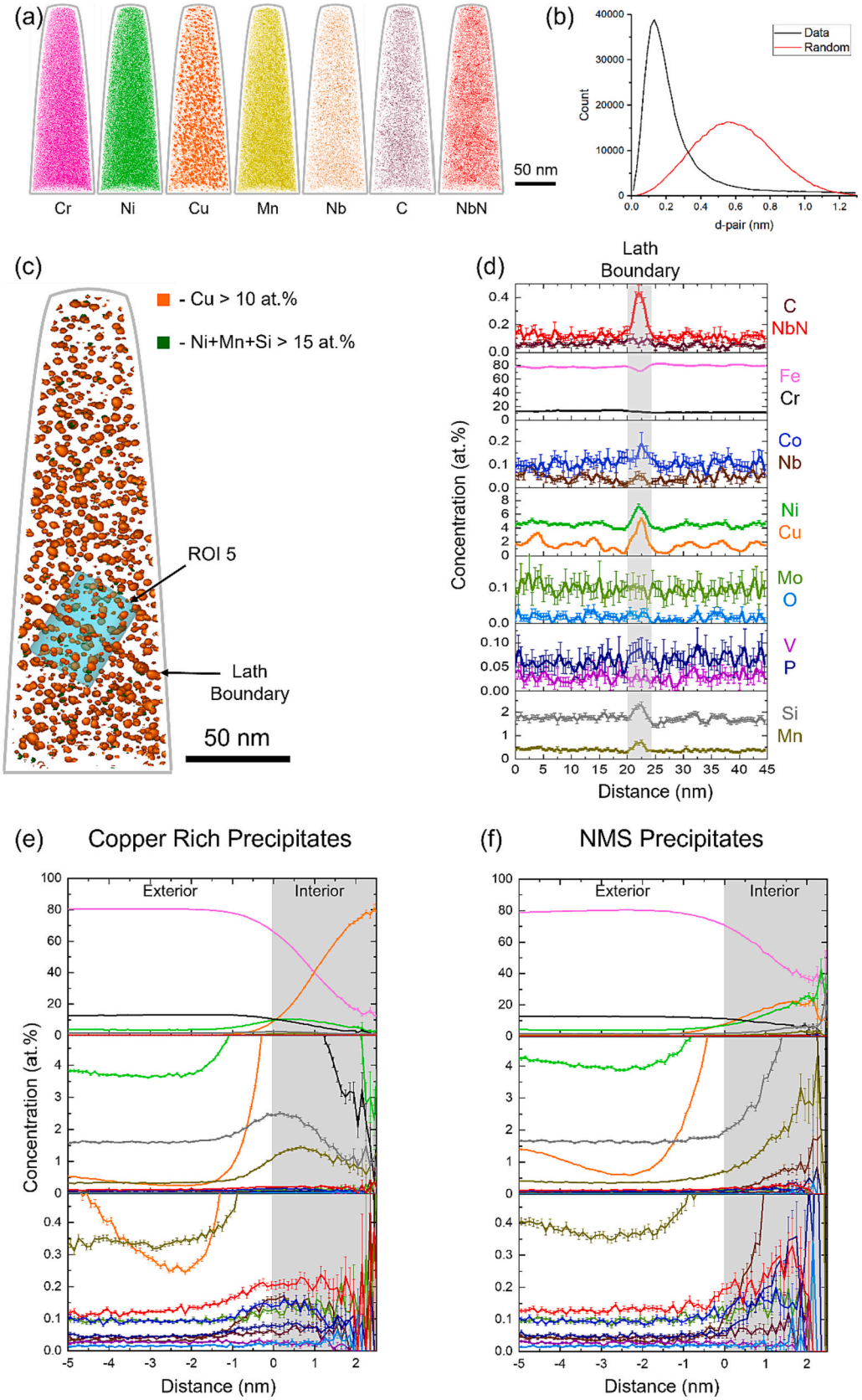


Fig. 8. APT data from the Low N 17–4 sample heat treated to the CA-H900 condition. (b) Cu nearest neighbour distribution (black) compared to a randomised distribution (red). (c) 10 at.% Cu isosurfaces (orange) and 15 at.% Ni, Mn, Si isosurfaces (green). (d) 1D concentration profile along the region of interest (ROI) across the lath boundary indicated in (c) (ROI 5). Concentration proxigrams of the Cu isosurfaces and the Ni, Mn, Si isosurfaces are shown in (e) and (f), respectively. (For interpretation of the references to colour in this figure legend, the reader is referred to the web version of this article.)

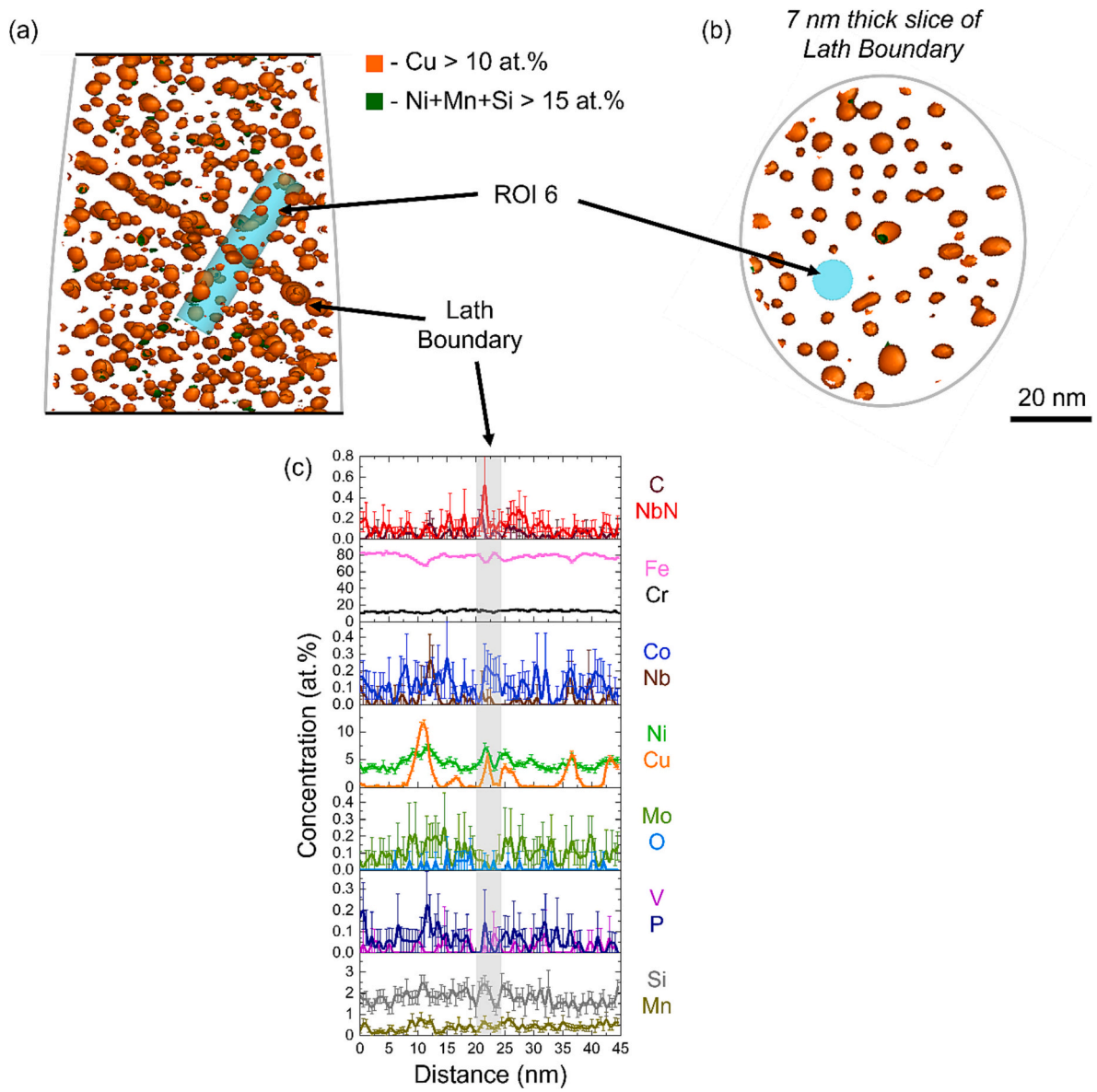


Fig. 9. Additional analysis on the lath boundary captured in the Low N 17–4 CA-H900 dataset. (a,b) Position of region of interest within the dataset showing that this ROI (ROI 6) avoids any lath boundary CRPs and NMS precipitates. (c) 1D concentration profile along region of interest (bottom to top).

7. It should be noted that not all elements detected within the build (Table 1) are presented in the analysis in Fig. 10 as the ROIs do not encompass a sufficient atomic count of the elements at lower concentration levels for any meaningful analysis. As shown by the proxigram in Fig. 8c, only Cu reaches its peak concentration within the CRP. Within the adjacent NMS precipitate, Ni, Si, Mn, and Nb all show peak concentrations. This can be contrasted with similar analysis for a CRP which formed on its own without adjacent co-precipitation of an NMS precipitate, shown in Fig. 10c and Fig. 10d. Fig. 10d shows that the peak concentrations for Ni, Nb, and Mn occur within the CRP, not adjacent to it. However, the relative concentrations of these elements are lower than those recorded in the NMS portion of the co-precipitate in Fig. 10b. It follows that, during the formation of CRPs upon aging, the elements constituting NMS precipitates diffuse into the CRP as this will reduce the interfacial energy of the precipitate with the matrix [13]. Once these elements reach a sufficiently high concentration, they begin to diffuse out of the existing CRP to form a new NMS precipitate. This is consistent with APT studies on the precipitation behaviour on the aging of wrought 17–4 PH stainless steel [10,13].

3.3. Comparison between the microstructural behaviour of high N 17-4 and Low N 17-4

Fig. 11 shows a schematic diagram of the microstructural evolution, as described in the preceding sections, of the two variants of LPBF 17–4 PH considered in this work. It can be seen that, in the as-built state, both variants exhibit δ-ferritic microstructures from solidification [14,15], with the High N 17–4 variant having a tendency to form a small volume fraction (~1% according to the EBSD results in Fig. 2) of austenite grains at δ-ferrite grain boundaries. In contrast, the Low N 17–4 variant has no detectable austenite in the as-built condition. It is determined by Thermocalc® (Fig. S 4 in the supplementary material) that both materials are fully austenitic at 1040 °C before the water quench during the CA heat treatment. In CA, the Low N 17–4 variant exhibits a fully martensitic microstructure, as would be expected from conventionally produced 17–4 PH [1–3]. However, the High N 17–4 variant shows a high volume fraction of retained austenite after quenching (~25% by the EBSD results in Fig. 2). After both variants are aged to the CA-H900 condition, the Low N 17–4 PH shows a high amount of Cu precipitation homogenously distributed in the martensitic matrix (Fig. 8a-c). However, the

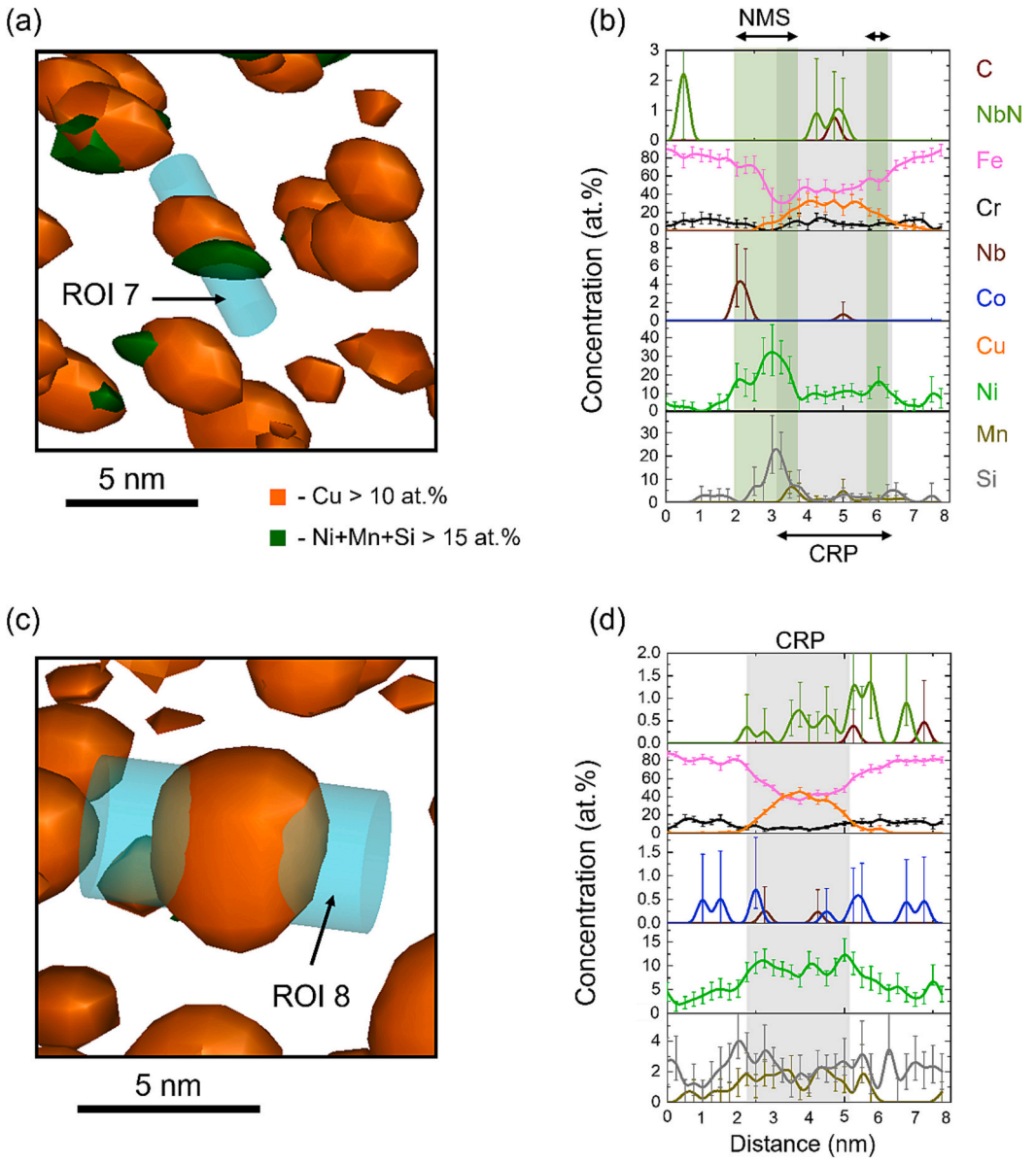


Fig. 10. 1D concentration profiles through (a,b) Cu and NMS precipitates (c,d) an isolated Cu precipitate within the Low N 17–4 CA-H900 dataset. (a,c) ROIs through precipitates used to create the 1D concentration profiles. (b,d) Concentration along the defined ROIs.

High N 17–4 does not show any bulk precipitation of CRPs in either the austenite or the martensite phases. Small CRPs (relative to those formed in the Low N 17–4 in the same heat treatment condition) have formed on the austenite/martensite phase boundaries only.

This difference in microstructural evolution between the two 17–4 PH builds has knock on effects on the mechanical properties. Fig. 12 shows the progression of each variant's hardness following the standard heat treatment sequence. The Low N 17–4 experiences a slight increase in hardness between the as-built and CA heat treatment states as a refined martensitic microstructure is formed. After the H900 aging treatment, the Low N 17–4 experiences a significant increase in hardness (~140 HV 5) correlating with the formation of a fine dispersion of CRPs, as shown in Fig. 8 and Fig. 11. Contrastingly, the hardness of the High N 17–4 decreases with the CA heat treatment, likely due to the introduction of a high volume fraction of the softer austenite phase and relieving of residual stress. The H900 aging treatment does not result in any discernible change in the hardness of the High N 17–4 as the bulk precipitation of CRPs has not occurred (shown in Fig. 4 and Fig. 11). It may be noted that the High N 17–4 has the greater as-built hardness, which may be resultant from effects unrelated to austenite retention after annealing or precipitation, such as the prevalence of defects, the retained volume fraction of δ-ferrite, or the relative strengths of dislocation interactions with cell boundaries [16,21,49]. However, the progression in mechanical properties following heat treatment is of greater interest to this research. Furthermore, the effect of age hardening has made the Low N 17–4 in the CA-H900 condition even harder than the High N material in the as-built condition due to the strong effect of precipitate hardening via the formation of Cu precipitates.

The understanding of the difference in composition and microstructural evolution of these two 17–4 PH builds, shown schematically in Fig. 11, and its resultant effect on their mechanical behaviours following standard heat treatments for this material, shown in Fig. 12, demonstrates that compositional variations incurred during the typical LPBF process flow can have unintended consequences on the resultant engineering part, effectively degrading the attractive property profile of this alloy.

It remains important to establish the mechanism by which Cu precipitation in the bulk of martensite laths in the High N 17–4 remains

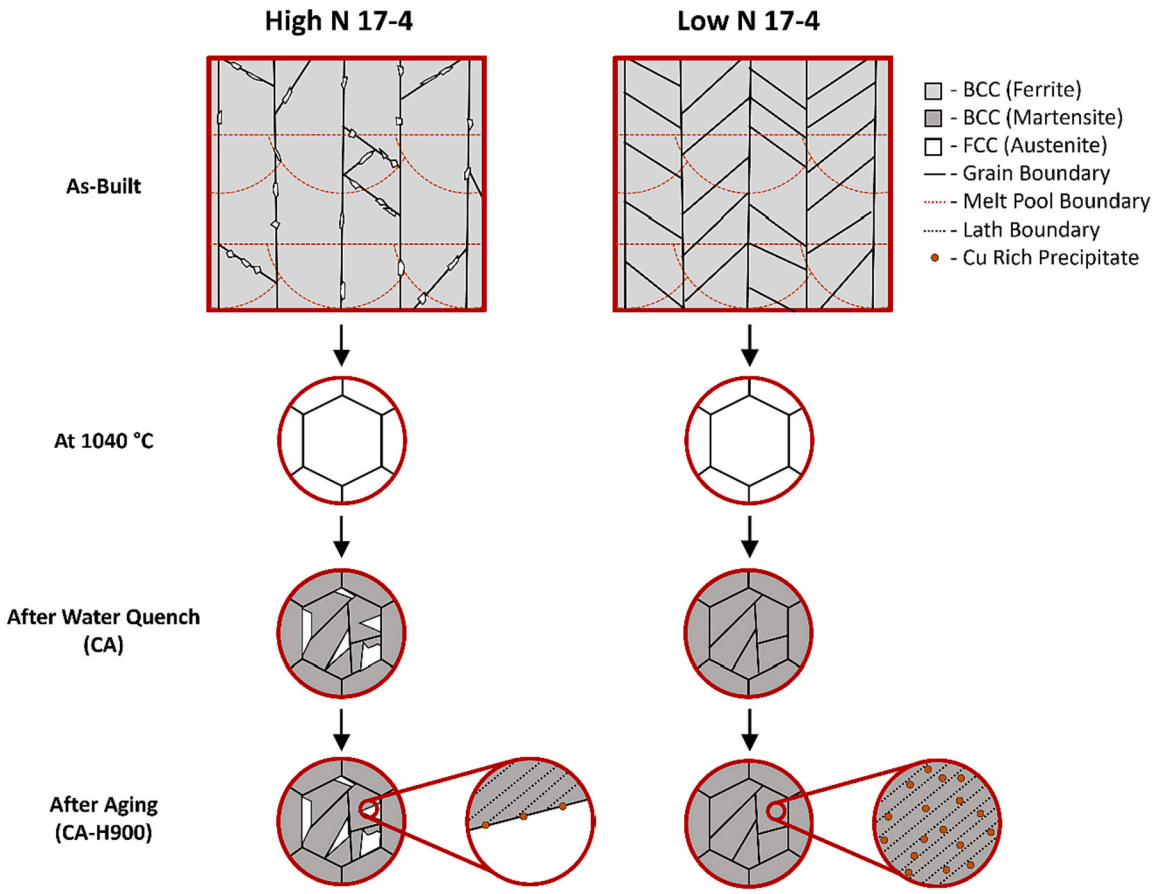


Fig. 11. Schematic microstructures of the High N 17–4 and Low N 17–4 variants in the as-built state and their evolution following the heat treatments considered in this research.

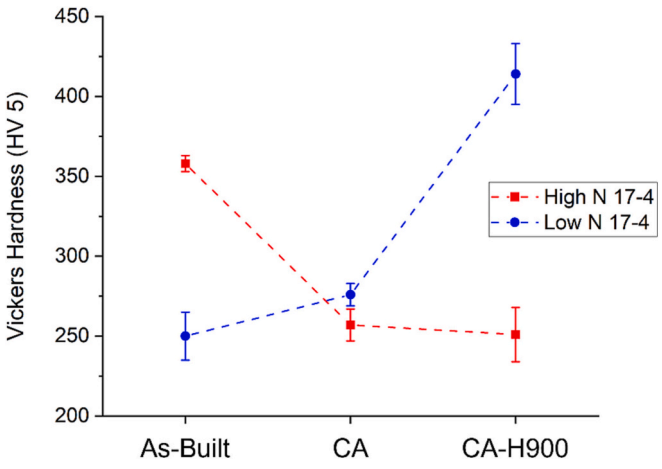


Fig. 12. Hardness testing results for both the High N 17–4 and Low N 17–4 in each heat treatment condition.

completely absent, as this effect has such a deleterious influence on the mechanical properties. Previous works [8,20,21,24,25] have stated that, as Cu has a greater solubility in austenite than in ferrite or martensite, the reduction in precipitate hardening behaviour on the macro-scale would result from Cu remaining in a solid solution in the austenite rather than precipitating out in martensite or ferrite. However, Fig. 4g and h show that there is no clustering or precipitation in either the martensite or austenite phases after the heat treatment. Furthermore, Fig. 4d shows that the concentration of Cu away from the phase boundary is equal and homogeneous between phases. This demonstrates that Cu does not diffuse from martensite to austenite during aging, meaning that this effect is not causing the absence of precipitation in martensite, as is suggested in literature [20,25].

In the High N 17–4 material, there is a high density of FCC/BCC phase boundaries after the CA heat treatment (Fig. 2f). Cu precipitates are found to form on these boundaries after aging High N 17–4 to the CA-H900 condition (Fig. 4c). It might, therefore, be reasoned that Cu has diffused to these phase boundaries to form precipitates heterogeneously rather than precipitating homogeneously out of bulk BCC regions of the microstructure. However, examining the Cu distribution across a phase boundary region devoid of distinct Cu precipitates in Fig. 4d, it can be seen that the Cu concentration is homogenous (at ~3.5 at.%) in the interior of both the FCC and BCC grains at regions >3 nm away from the boundary. This means that at regions >3 nm from this interface there has been no diffusional loss of Cu meaning that any attraction of Cu to phase boundaries would not inhibit Cu precipitation in the martensite. Additionally, if any longer range diffusion of Cu to the phase boundary had taken place during aging, it would be expected that there would be a lower bulk concentration of Cu in the austenite grain than in the BCC martensite lath as the diffusivity of Cu in austenite is ~10^3 times greater [25]. The fact that bulk concentration of Cu between austenite and martensite are shown to be the same in Fig. 4d suggests such diffusion does not take place during aging.

Another possibility would be that Cu and N form interstitial-substitutional complexes within the matrix as discussed in [50], inhibiting the formation of Cu precipitates upon aging. However, Cu-NbN nearest neighbour analysis of the site-specific CA-H900 APT data (shown in Fig. S 5) do not show any co-segregation behaviour. In fact, if any such complexes were being formed between Cu and any other

elements, this would have a resultant effect on the Cu—Cu NN distributions, resulting in the appearance of clustering in Fig. 2l and Fig. 4h.

Finally, Thermocalc® was used to analyse whether the difference in composition between the two materials resulted in a difference in Cu precipitation kinetics. This analysis (Fig. S 6 in the supplementary material) did not reveal any appreciable difference in the diffusivity of Cu in a BCC matrix between the High N 17–4 and Low N 17–4 build compositions at the aging temperature of 480 °C. Additional research is recommended to determine the cause of the High N 17–4 variant's absence of bulk precipitation behaviour.

4. Conclusions

In the present work, the microstructural evolution of two variants of LPBF fabricated 17–4 PH stainless steel samples with significantly different N compositions resultant from different powder feedstocks and fabrication pathways was studied in the as-built and various typical heat treated states. A systematic study of the effect of these compositional differences on the heat treatment response, solute clustering, precipitation behaviour, and hardness evolution was conducted. The key findings of this study are summarised as follows.

1. Due to compositional differences, High N 17–4 samples had a duplex austenitic / martensitic matrix following solution annealing (condition A/CA heat treatment) whereas the same heat treatment resulted in a ~ 100% martensitic microstructure in Low N 17–4 samples.
2. In the as-built High N 17–4 samples, there is a distinct compositional difference between the austenite and ferrite phases resultant from the intrinsic heat treatment associated with the AM process, with the austenite being enriched in C, N, Ni, Cu, O, and Co and the ferrite being enriched in only Fe. However, following the CA-H900 thermal processing route, there is no discernible difference in the bulk composition between austenite and martensite.
3. Thermal aging of the duplex microstructures of the High N 17–4 CA samples did not result in Cu precipitation in either phase. Cu precipitates are only observed to form at the boundaries between BCC and FCC grains in High N 17–4 in both the as-built and CA-H900 conditions.
4. Low N 17–4 samples showed little to no austenite in the as-built state. Intrinsic heat treatment has been found to result in a degree of Cu precipitation in the Low N 17–4 as-built sample, though not to the degree of the aged (CA-H900) sample.
5. The Low N 17–4 samples exhibited the expected behaviour of Cu within the matrix upon aging. The CA heat treatment resulted in a random distribution of Cu within the resultant martensitic matrix. Performing the H900 aging treatment resulted in the desirable formation of nanoscale Cu precipitates throughout the martensitic lath interiors. In the H900 condition, Cu precipitates formed with an average diameter of 3.8 nm and an average number density of 1.30×10^{23} m^{-3} (this needs to change to 1.89×10^{23} m^{-3}). The Cu precipitates also showed enrichment in Ni, Mn, Si, and Nb. When these elements became sufficiently enriched, they formed their own phase co-precipitating with existing Cu precipitates.
6. In the Low N 17–4 CA-H900 sample, segregation at lath boundaries was observed, largely because of the nucleation of precipitates at those lath boundaries. This resulted in a high density of Cu precipitates at the boundary itself surrounded by a region depleted in Cu and other alloying elements.
7. High N 17–4 showed no increase in hardness with aging, whereas the Low 17–4 showed a ~ 140 HV 5 increase in hardness after the H900 aging treatment. This correlated well with the observed precipitation behaviour in both builds.

Overall, this work demonstrates that compositional effects on phase transformation pathways can lead to the absence of precipitate hardening behaviour in LPBF 17–4 PH stainless steel, effectively degrading the attractive property profile of this alloy. However, we have also shown that desirable phase transformation pathways, comparable to wrought, can be achieved if these compositional variations are managed during the LPBF process flow. This is important for the reproducibility of engineering LPBF parts.

CRediT authorship contribution statement

M.S. Moyle: Writing – original draft, Methodology, Investigation, Formal analysis, Conceptualization. **N. Haghdadi:** Writing – review & editing, Supervision, Methodology, Conceptualization. **F. Theska:** Writing – review & editing, Methodology, Investigation, Formal analysis. **M.P. Haines:** Writing – review & editing, Investigation, Formal analysis. **X.Z. Liao:** Writing – review & editing, Project administration, Funding acquisition. **S.P. Ringer:** Writing – review & editing, Resources, Project administration, Funding acquisition. **S. Primig:** Writing – review & editing, Supervision, Resources, Project administration, Methodology, Funding acquisition, Conceptualization.

Declaration of competing interest

The authors declare that they have no known competing financial interests or personal relationships that could have appeared to influence the work reported in this paper.

Data availability

Data will be made available on request.

Acknowledgments

Funding by the AUSMURI program, Department of Industry, Innovation and Science, Australia is gratefully acknowledged. The authors acknowledge the facilities, scientific, and technical support provided at the Electron Microscope Unit, UNSW Sydney (Mark Wainwright Analytical Centre), as well as Sydney Microscopy & Microanalysis (SMM) at the University of Sydney — both nodes of Microscopy Australia, a national research facility supported under the Commonwealth NCRIS program.

Appendix A. Supplementary data

Supplementary data to this article can be found online at https://doi.org/10.1016/j.matchar.2024.113768.

References

[1] S. Cheruvathur, E.A. Lass, C.E. Campbell, Additive manufacturing of 17-4 PH stainless steel: post-processing heat treatment to achieve uniform reproducible microstructure, JOM 68 (2016) 930–942, https://doi.org/10.1007/s11837-015-1754-4.
[2] C.N. Hsiao, C.S. Chiou, J.R. Yang, Aging reactions in a 17-4 PH stainless steel, Mater. Chem. Phys. 74 (2002) 134–142.
[3] C.F. Arisoy, G. Bas, M.S. Kelami, Failure of a 17–4 PH Stainless Steel Sailboat Propeller Shaft 10, 2003, pp. 711–717, https://doi.org/10.1016/S1350-6307(03)00041-4.
[4] L.E. Murr, E. Martinez, J. Hernandez, S. Collins, K.N. Amato, S.M. Gaytan, P. W. Shindo, Microstructures and properties of 17-4 PH stainless steel fabricated by selective laser melting, J. Mater. Res. Technol. 1 (2012) 167–177.
[5] B.L. Facchini, V. Jr, I. Lonardelli, E. Magalini, P. Robotti, A. Molinari, Metastable austenite in 17–4 precipitation-hardening stainless steel produced by selective laser melting, Adv. Eng. Mater. (2010) 184–188, https://doi.org/10.1002/adem.200900259.
[6] L.E. Murr, E. Martinez, K.N. Amato, S.M. Gaytan, J. Hernandez, D.A. Ramirez, P. W. Shindo, F. Medina, R.B. Wicker, Fabrication of metal and alloy components by additive manufacturing: examples of 3D materials science, J. Mater. Res. Technol. 1 (2012) 42–54, https://doi.org/10.1016/S2238-7854(12)70009-1.
[7] U.K. Viswanathan, S. Banerjee, R. Krishnan, Effects of aging on the microstructure of 17-4 PH stainless steel, Mater. Sci. Eng. 104 (1988) 181–189, https://doi.org/10.1016/0025-5416(88)90420-X.

[8] M. Murayama, Y. Katayama, K. Hono, Microstructural evolution in a 17-4 PH stainless steel after aging at 400 °C, Metall. Mater. Trans. A Phys. Metall. Mater. Sci. 30 (1999) 345–353, https://doi.org/10.1007/s11661-999-0323-2.

[9] ASM International Handbook Committee, Heat treating of stainless steels, in: ASM Handbook Vol. 4, Heat Treating, ASM International, 1991, pp. 769–792, https://doi.org/10.31399/asm.tb.pht2.t51440175.

[10] Z. Wang, H. Li, Q. Shen, W. Liu, Z. Wang, Nano-precipitates evolution and their effects on mechanical properties of 17-4 precipitation-hardening stainless steel, Acta Mater. 156 (2018) 158–171, https://doi.org/10.1016/j.actamat.2018.06.031.

[11] G. Han, Z.J. Xie, Z.Y. Li, B. Lei, C.J. Shang, R.D.K. Misra, Evolution of crystal structure of Cu precipitates in a low carbon steel, Mater. Des. 135 (2017) 92–101, https://doi.org/10.1016/j.matdes.2017.08.054.

[12] H. Sun, W. Lv, Y. Yang, D. Li, L. Yan, X. Pang, Y. He, K. Gao, Optimizing the hydrogen embrittlement resistance by tuning the structures of Cu-rich nanoprecipitates in high strength martensite stainless steels, Acta Mater. 246 (2023) 118722, https://doi.org/10.1016/j.actamat.2023.118722.

[13] G. Yeli, M.A. Auger, K. Wilford, G.D.W. Smith, P.A.J. Bagot, M.P. Moody, Sequential nucleation of phases in a 17-4PH steel: microstructural characterisation and mechanical properties, Acta Mater. 125 (2017) 38–49, https://doi.org/10.1016/j.actamat.2016.11.052.

[14] M. Alnajjar, F. Christien, K. Wolski, C. Bosch, Evidence of austenite by-passing in a stainless steel obtained from laser melting additive manufacturing, Addit. Manuf. 25 (2019) 187–195, https://doi.org/10.1016/j.addma.2018.11.004.

[15] M.S. Moyle, N. Haghdadi, X.Z. Liao, S.P. Ringer, S. Primig, On the microstructure and texture evolution in 17-4 PH stainless steel during laser powder bed fusion: towards textural design, J. Mater. Sci. Technol. 117 (2022) 183–195, https://doi.org/10.1016/j.jmst.2021.12.015.

[16] N. Haghdadi, M. Laleh, M. Moyle, S. Primig, Additive manufacturing of steels: a review of achievements and challenges, J. Mater. Sci. 56 (2020) 64–107, https://doi.org/10.1007/s10853-020-05109-0.

[17] 17-4 PH Stainless Steel: Product Data Bulletin, AK Steel Corporation, 2018, p. 1.

[18] D.J. Shaffer, A.E. Wilson-Heid, J.S. Keist, A.M. Beese, T.A. Palmer, Impact of retained austenite on the aging response of additively manufactured 17-4 PH grade stainless steel, Mater. Sci. Eng. A 817 (2021) 141363, https://doi.org/10.1016/j.msea.2021.141363.

[19] E.A. Lass, M.R. Stoudt, M.E. Williams, Additively manufactured nitrogen-atomized 17-4 PH stainless steel with mechanical properties comparable to wrought, Metall. Mater. Trans. A Phys. Metall. Mater. Sci. 50 (2019) 1619–1624, https://doi.org/10.1007/s11661-019-05124-0.

[20] T. LeBrun, T. Nakamoto, K. Horikawa, H. Kobayashi, Effect of retained austenite on subsequent thermal processing and resultant mechanical properties of selective laser melted 17-4 PH stainless steel, Mater. Des. 81 (2015) 44–53, https://doi.org/10.1016/j.matdes.2015.05.026.

[21] T. DebRoy, H.L. Wei, J.S. Zuback, T. Mukherjee, J.W. Elmer, J.O. Milewski, A. M. Beese, A. Wilson-Heid, A. De, W. Zhang, Additive manufacturing of metallic components – Process, structure and properties, Prog. Mater. Sci. 92 (2018) 112–224, https://doi.org/10.1016/j.pmatsci.2017.10.001.

[22] S. Sabooni, A. Chabok, S.C. Feng, H. Blaauw, T.C. Pijper, H.J. Yang, Y.T. Pei, Laser powder bed fusion of 17-4 PH stainless steel: a comparative study on the effect of heat treatment on the microstructure evolution and mechanical properties, Addit. Manuf. 46 (2021) 102176, https://doi.org/10.1016/j.addma.2021.102176.

[23] H. Bhadeshia, R. Honeycombe, Steels: Microstructure and Properties, 4th ed., Butterworth-Heinemann, 2017.

[24] T.-H. Hsu, Y.-J. Chang, C.-Y. Huang, H.-W. Yen, C.-P. Chen, K.-K. Jen, A.-C. Yeh, Microstructure and property of a selective laser melting process induced oxide dispersion strengthened 17-4 PH stainless steel, J. Alloys Compd. 803 (2019) 30–41, https://doi.org/10.1016/j.jallcom.2019.06.289.

[25] G. Salje, M. Feller-Kniepmeier, The diffusion and solubility of copper in iron, J. Appl. Phys. 48 (1977) 1833–1839, https://doi.org/10.1063/1.323934.

[26] Z. Xu, X. Shen, T. Allam, W. Song, W. Bleck, Austenite reversion and nano-precipitation during a compact two-step heat treatment of medium-Mn steel containing Cu and Ni, J. Mater. Res. Technol. 17 (2022) 2601–2613, https://doi.org/10.1016/j.jmrt.2022.02.008.

[27] E. Jägle, Z. Sheng, P. Kürnsteiner, S. Ocylok, A. Weisheit, D. Raabe, Comparison of maraging steel micro- and nanostructure produced conventionally and by laser additive manufacturing, Materials 10 (2016) 8, https://doi.org/10.3390/ma10010008.

[28] M. Shirdel, H. Mirzadeh, M.H. Parsa, Nano/ultrafine grained austenitic stainless steel through the formation and reversion of deformation-induced martensite: mechanisms, microstructures, mechanical properties, and TRIP effect, Mater. Charact. 103 (2015) 150–161, https://doi.org/10.1016/j.matchar.2015.03.031.

[29] B. Gault, M.P. Moody, J.M. Cairney, S.P. Ringer, Atom probe crystallography, Mater. Today 15 (2012) 378–386, https://doi.org/10.1016/S1369-7021(12)70164-5.

[30] K. Babinsky, R. De Kloe, H. Clemens, S. Primig, A novel approach for site-specific atom probe specimen preparation by focused ion beam and transmission electron backscatter diffraction, Ultramicroscopy 144 (2014) 9–18, https://doi.org/10.1016/j.ultramic.2014.04.003.

[31] M.S. Moyle, N. Haghdadi, W.J. Davids, X.Z. Liao, S.P. Ringer, S. Primig, Evidence of in-situ Cu clustering as a function of laser power during laser powder bed fusion of 17–4 PH stainless steel, Scr. Mater. 219 (2022) 114896, https://doi.org/10.1016/j.scriptamat.2022.114896.

[32] E.A. Jägle, Z. Sheng, L. Wu, L. Lu, J. Risse, A. Weisheit, D. Raabe, Precipitation reactions in age-hardenable alloys during laser additive manufacturing, JOM 68 (2016) 943–949, https://doi.org/10.1007/s11837-015-1764-2.

[33] Z. Wang, X. Fang, H. Li, W. Liu, Atom probe tomographic characterization of nanoscale Cu-rich precipitates in 17-4 precipitate hardened stainless steel tempered at different temperatures, Microsc. Microanal. 23 (2017) 340–349, https://doi.org/10.1017/S1431927616012629.

[34] Y.Y. Chuang, R. Schmid, Y.A. Chang, Thermodynamic analysis of the iron-copper system I: the stable and metastable phase equilibria, Metall. Trans. A. 15 (1984) 1921–1930, https://doi.org/10.1007/BF02664905.

[35] S.D. Meredith, J.S. Zuback, J.S. Keist, T.A. Palmer, Impact of composition on the heat treatment response of additively manufactured 17-4 PH grade stainless steel, Mater. Sci. Eng. A 738 (2018) 44–56, https://doi.org/10.1016/j.msea.2018.09.066.

[36] H.R. Lashgari, C. Kong, E. Adabifiroozjaei, S. Li, Microstructure, post thermal treatment response, and tribological properties of 3D printed 17-4 PH stainless steel, Wear 457 (2020) 203367, https://doi.org/10.1016/j.wear.2020.203367.

[37] Z. Nishiyama, X-ray investigation of the mechanism of the transformation from face-centerd cubic lattice to body-centerd cubic lattice, Sci. Tohoku Univ. 23 (1934).

[38] G. Wassermann, Ueber den Mechanismus der [alpha]-[gamma]-Umwandlung des Eisens, Verlag Stahleisen (n.d.).

[39] W. Pitsch, Der orientierungszusammenhang zwischen zementit und austenit, Acta Metall. 10 (1962) 897–900.

[40] B. Gault, M.P. Moody, J.M. Cairney, S.P. Ringer, Atom Probe Microscopy, Springer Science & Business Media, 2012, https://doi.org/10.1007/978-1-4614-3436-8_6.

[41] D.A. Porter, K.E. Easterling, M.Y. Sherif, Phase Transformatinos in Metals and Alloys, Third, CRC Press, 2009.

[42] P. Lejček, Grain Boundary Segregation in Metals, Springer, 2010, https://doi.org/10.1007/978-3-642-12505-8_1.

[43] E.J. Seo, L. Cho, J.K. Kim, J. Mola, L. Zhao, S. Lee, B.C. De Cooman, Focused ion beam-induced displacive phase transformation from austenite to martensite during fabrication of quenched and partitioned steel micro-pillar, J. Alloys Compd. 812 (2020) 152061, https://doi.org/10.1016/j.jallcom.2019.152061.

[44] G. Kurdjumow, G. Sachs, Uber den Mechanismus der Stahlhartung, Zeitschrift Fur Physik 64 (1930) 325–343, https://doi.org/10.1007/BF01397346.

[45] G.E. Dieter, Mechanical Metallurgy, McGraw-Hill, New York, 1961.

[46] M.F. Ashby, D.R.H. Jones, Engineering Materials 1: An Introduction to Properties, Applications, and Design, 4th ed., Butterworth-Heinemann, 2012.

[47] P.J. Clemm, J.C. Fisher, The influence of grain boundaries on the nucleation of secondary phases, Acta Metall. 3 (1955) 70–73.

[48] P.J. Othen, M.L. Jenkins, G.D.W. Smith, High-resolution electron microscopy studies of the structure of Cu precipitates in α-Fe, Philos. Mag. A: Phys. Condens. Matter. Struct. Defects Mech. Prop. 70 (1994) C1–24, https://doi.org/10.1080/01418619408242533.

[49] Y.M. Wang, T. Voisin, J.T. McKeown, J. Ye, N.P. Calta, Z. Li, Z. Zeng, Y. Zhang, W. Chen, T.T. Roehling, R.T. Ott, M.K. Santala, P.J. Depond, M.J. Matthews, A. V. Hamza, T. Zhu, Additively manufactured hierarchical stainless steels with high strength and ductility, Nat. Mater. 17 (2018) 63–70, https://doi.org/10.1038/NMAT5021.

[50] K. Oda, N. Kondo, K. Shibata, X-ray absorption fine structure analysis of interstitial (C, N)-substitutional (Cr) complexes in austenitic stainless steels, ISIJ Int. 30 (1990) 625–631, https://doi.org/10.2355/isijinternational.30.625.